arXiv:2501.08423v3 [stat.ML] 6 May 2025

LILAN: A LINEAR LATENT NETWORK APPROACH FOR REAL-TIME SOLUTIONS OF STIFF NONLINEAR ORDINARY DIFFERENTIAL EQUATIONS

William Cole Nockolds
Oden Institute for Computational Engineering and Sciences,
University of Texas at Austin
Austin, TX 78712
cole.nockolds@utexas.edu

C G Krishnanunni
Dept of Aerospace Engineering & Engineering Mechanics,
University of Texas at Austin
Austin, TX 78712
krishnanunni@utexas.edu

Tan Bui-Thanh
Oden Institute for Computational Engineering and Sciences,
Dept of Aerospace Engineering & Engineering Mechanics,
University of Texas at Austin
Austin, TX 78712
tanbui@oden.utexas.edu

Xianzhu Tang
Theoretical Division, Los Alamos National Laboratory
Los Alamos, NM 87545, United States of America
xtang@lanl.gov

ABSTRACT

Solving stiff ordinary differential equations (StODEs) requires sophisticated numerical solvers, which are often computationally expensive. In general, traditional explicit time integration schemes with restricted time stepsizes are not suitable for StODEs, and one must resort to costly implicit methods to compute solutions. On the other hand, state-of-the-art machine learning (ML) based methods such as Neural ODE (NODE) poorly handle the timescale separation of various elements of the solutions to StODEs, while still requiring expensive implicit/explicit integrations at inference time. In this work, we propose a linear latent network (Lilan) approach in which the dynamics in the latent space can be integrated analytically, and thus numerical integration is completely avoided. At the heart of Lilan are the following key ideas: i) two encoder networks to encode initial condition together with parameters of the ODE to the slope and the initial condition for the latent dynamics, respectively. Since the latent dynamics, by designed, are linear, the solution can be evaluated analytically; ii) a neural network to map initial condition, parameters, and the physical time to latent times, one for each latent variable. Intuitively, this allows for the "stretching/squeezing" of time in the latent space, thereby allowing for varying levels of attention to different temporal scales in the solution; and iii) a decoder network to decode the latent solutions the physical solution at the corresponding physical time. We provide a universal approximation theorem for the proposed Lilan approach, showing that it can approximate the solution of any stiff nonlinear system on a compact set to any

degree of accuracy ε. We also show that the dimension of the latent dynamical system in `Lilan` is independent of ε. Numerical results on "Robertson Stiff Chemical Kinetics Model" [1] and "Plasma Collisional-Radiative Model" [2] suggest that `Lilan` outperforms state-of-the-art machine learning approaches for handling StODEs. Numerically, we also show that `Lilan` outperforms other machine learning methods on multiple partial differential equations (PDEs) with known stiff behaviors, such as the "Allen-Cahn" and "Cahn-Hilliard" PDEs [3].

***K*eywords** Stiff ordinary differential equations · Stiff partial differential equations · Surrogate modeling · Latent dynamics · encoder and decoder neural networks

1 Introduction

Stiff ordinary differential equations (StODEs), arising in many scientific and engineering disciplines, pose unique challenges for numerical integration. While a precise definition of stiffness has eluded mathematicians for decades, systems characterized by numerical stiffness typically have important behaviors on timescales that differ by several orders of magnitude. In order to realize these features and ensure that the solution remains bounded during numerical integration with explicit methods, extremely small time steps must be taken [4], making explicit integration prohibitively expensive. Several attempts to define a metric for stiffness have been made with the most popular being the stiffness ratio. The stiffness ratio compares the maximum magnitude real part eigenvalue to the minimum magnitude real part eigenvalue of the Jacobian matrix of a dynamical system [5, 6]. This ratio gives a comparison between the speed of the fastest and slowest evolving components of the solution at any temporal point in the integration. The expensive nature of solving StODEs necessitates the development of machine learning (ML) techniques for accelerating simulation of such systems.

In recent years, scientific machine learning techniques have been used to replace or drastically speed up traditional numerical solvers. However, stiff systems have proven challenging for integration with neural networks. It was shown in [7] that the gradient flow dynamics for training physics informed neural networks (PINNS) are typically stiff themselves, placing strict limitations on the gradient descent step size. Stiffness in gradient flow dynamics becomes particularly troublesome when the loss function contains multiple competing terms, which can lead to even greater magnitude variability in parameter gradients [7] and cause optimization to diverge.

Employing deep learning to learn discretized solutions of dynamical systems is gaining popularity in recent years [8, 9, 10]. In particular, Dikeman et al. [5] considers an approach of explicitly including an approximation of the stiffness ratio as a term in the loss function for a neural ODE type architecture. However, as mentioned previously, such soft constraints can lead to training difficulties. Another neural ODE style approach is described in [6], where the authors devise a scheme to scale each component of the neural ODE's output by unique factors derived from the magnitude of the data and integration interval. While the approach showed improvements over vanilla neural ODE, an expensive implicit solver was still necessary to integrate solutions. Kumar et al. [11] follows a similar approach, requiring an implicit solver, but instead of scaling factors, the authors improve the performance of neural ODEs for stiff problems by imposing explicit constraints for conservation of mass. Alternately, researchers have also considered modifying the physics informed neural network (PINN) architecture to solve stiff problems. Ji et al. [12] illustrates a method utilizing quasi-steady state assumptions (QSSA) to convert a stiff system into one that is non-stiff and thus easier for PINNS to handle. However, results from this paper show that QSSA conversion, which works by removing the fastest evolving components of the solution, will cause some behaviors of the original system to be lost. While many approaches designed to alleviate the challenges of integrating stiff systems using neural networks have shown impressive results and improvements over traditional machine learning approaches, finding an approach that fully preserves all aspects of the original system and does not necessitate an implicit solver remains an open question.

Yet another approach to simulate dynamical systems involves the use of autoencoders to learn a latent dynamical system, typically of lower dimensionality than the original system, that can be easily solved and decoded to recover the original solution using trained decoders [5, 10, 13, 14, 15]. This approach can be useful because it makes the evolution of the state computationally inexpensive since operations take place on the low dimensional latent representation. However, without a good estimate of the intrinsic dimensionality of the system, important information could be lost in the encoding process [16]. On the other hand, some new approaches propose increasing the dimension of the state through nonlinear featurization. In the area of reservoir computing, methods that utilize high dimensional "reservoir" representations of data have shown promise in the integration of stiff and even chaotic systems [17, 1, 18]. In the reinforcement learning (RL) community, augmenting the state vector with nonlinear featurization has been shown to improve the training of RL algorithms for certain tasks [19].

In this work, we developed an autoencoder-based approach to accelerate the simulation of StODEs. Our approach follows the intuition that given a stiff dynamical system, it may be possible to learn a higher dimensional latent

dynamical system which is non-stiff and therefore easier to integrate. In particular, we utilize an encoder that takes in the initial condition of the original dynamical system and outputs the initial condition for latent dynamics. By implicitly imposing a constant velocity latent dynamics structure, we completely evade numerical integration in the latent space since the solution is a sequence of fully linear trajectories and can therefore be computed analytically. The trained decoder can then retrieve, from the latent representation, the solution to the original dynamics, as and when required. Our theoretical analysis reveals that one can approximate the solution of a stiff, nonlinear system on a compact set to any degree of accuracy, ε, using our latent space approach, and that the required dimension of the latent space is independent of ε. Additionally, our theoretical analysis suggests employing a nonlinear transformation on the time variable allows for "stretching/squeezing" time in the latent space, thereby allowing for varying levels of attention to different temporal regions of the solution. Our experiments on the "ROBER Stiff Chemical Kinetics Model" [1] and the "Plasma Collisional-Radiative Model" [2] suggest that the proposed approach can outperform state-of-the-art ML approaches for calculating solutions to StODEs. Additionally, the approach outperforms other machine learning methods on multiple PDEs with known stiff behaviors, the "Allen-Cahn" and "Cahn-Hilliard" PDEs [3].

2 Mathematical framework

In this work, all matrices and vectors are represented in boldface. We consider the following autonomous parametrized StODE:

$$\frac{d\boldsymbol{x}}{dt} = \boldsymbol{f}_{\mathbf{p}}\left(\boldsymbol{x}(t)\right), \quad \boldsymbol{x}(0) = \boldsymbol{x}_0, \tag{1}$$

$\boldsymbol{f}_{\mathbf{p}} : \mathcal{G} \to \mathbb{R}^{n_x}$, where $\mathcal{G} \subset \mathbb{R}^{n_x}$ is a non-empty, open set, $\mathbf{p} \in \mathcal{X}_p$, where $\mathcal{X}_p \subset \mathbb{R}^{n_p}$ is a non-empty, compact set, and $\boldsymbol{x}_0 \in \mathcal{G}$. To discuss our proposed approach, let us first introduce the following definition.

Definition 1 *Flow map*

Define the set:

$$\mathcal{W} = \bigcup_{\boldsymbol{x}_0 \in \mathcal{G},\ \mathbf{p} \in \mathcal{X}_p} I_{\boldsymbol{x}_0;\mathbf{p}} \times \{\boldsymbol{x}_0\} \times \{\mathbf{p}\} \subseteq \mathbb{R} \times \mathcal{G} \times \mathcal{X}_p,$$

where $I_{\boldsymbol{x}_0;\mathbf{p}}$ is the maximal interval of existence of the solution[1] of (1) for a given $\boldsymbol{x}_0,\ \mathbf{p}$. We define the flow map (if it exists) to be the function $\boldsymbol{\psi}_{\boldsymbol{x}} : \mathcal{W} \to \mathcal{G}$ such that $\boldsymbol{\psi}_x\left(t, \boldsymbol{x}_0, \mathbf{p}\right) = \boldsymbol{x}(t)$, where $\boldsymbol{x}(t)$ solves (1) for a given $\{\boldsymbol{x}_0,\ \mathbf{p}\}$.

Our objective in this work is to develop a surrogate model for approximating the solution $\boldsymbol{x}(t)$, on some closed and bounded interval I, for any given $\mathbf{p} \in \mathcal{X}_p,\ \boldsymbol{x}_0 \in \mathcal{G}$ (assuming that $I \subseteq I_{\boldsymbol{x}_0;\mathbf{p}}$ for all $\mathbf{p},\ \boldsymbol{x}_0$). Therefore, it is easy to see that, what we aim is to learn a surrogate for the flow map $\boldsymbol{\psi}_x\left(t, \boldsymbol{x}_0, \mathbf{p}\right)$.

2.1 Motivation for the proposed approach

When dealing with stiff systems, it is clear that a neural ODE type approach can be quite expensive at inference time, since it involves using an implicit solver for integrating the resulting neural ODE, which may still produce a stiff system [6]. Leveraging the fact that under certain conditions on $\boldsymbol{f}_{\mathbf{p}}$ (lemma 1), the flow map in definition 1 is continuous, it is natural to consider learning a surrogate for the flow map. It is clear that if the flow map is continuous on a compact set, theoretically, one could use a single hidden layer neural network to learn the flow map to any degree of accuracy, ε, by the universal approximation theorem for neural networks [21]. Note that this procedure completely avoids numerical integration at inference time and provides an extremely cheap surrogate model. However, the highly nonlinear nature of the flow map presents a computationally challenging optimization problem for neural networks and exhibits poor generalization as we demonstrate in figure 1. In this work, we attempt to first learn a high dimensional latent dynamical system whose solution can be decoded to generate the the flow map associated with the original dynamics. Our numerical result suggests that this presents a computationally feasible optimization procedure for learning the flow map and exhibits better generalization as demonstrated in figure 1. Figure 1 (left) depicts the average point-wise relative error of predictions (see (49)) over time for a test dataset, with the proposed approach shown in blue, and a direct learning of the flow map, via one neural network, shown in orange. Note that both approaches have approximately the same number of learnable parameters. It is clear that our approach shows approximately one order of magnitude lower error than the direct learning approach. Additionally, viewing the loss curves in figure 1 (right), it is clear that the approach of directly learning the flow map via a single neural network is prone to overfitting the training data, which is demonstrated by the vast difference between the training and validation loss. Our method, however, has better generalization ability, as evident from figure 1 (right). We found that direct learning of the flow map can be effective for low-dimensional problems, however, as the dimension of the problem increases, it becomes too challenging for a single

[1] Refer to [20] for the definition of maximal interval of existence of the solution.

network to accurately predict the flow map, in comparison to our approach. Rigorous theoretical investigation on this aspect is a subject of future study (also see comments in section 5).

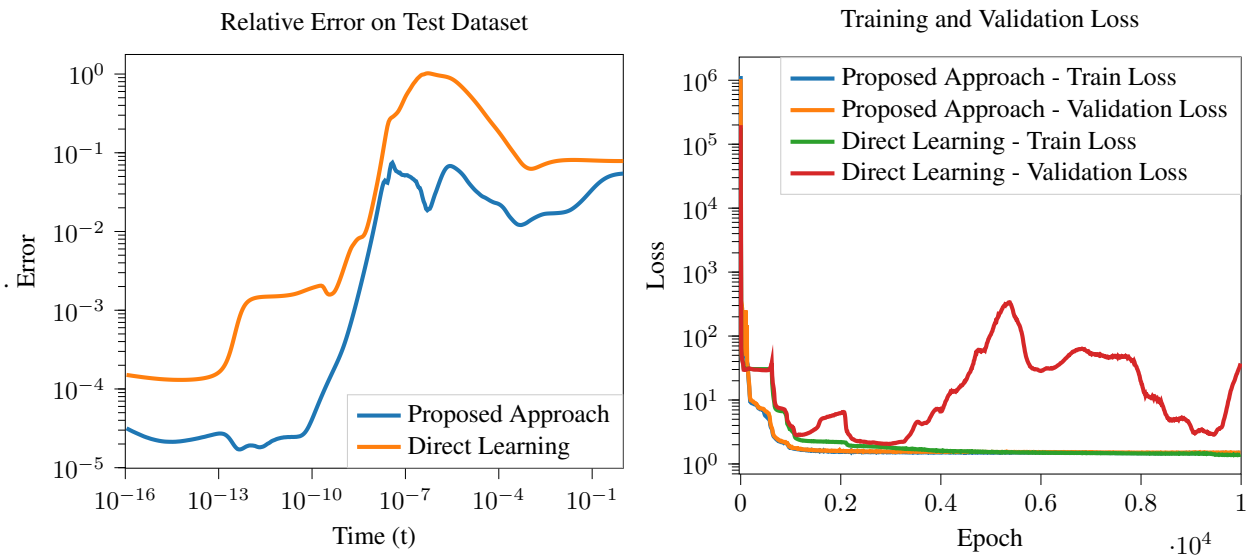

Figure 1: Learning flow map by our proposed approach vs. a direct learning approach. Left to Right: Average point-wise relative error (49) in predictions for the full CR model (section 3.2) on the test dataset; Training and validation loss curves for the two approaches.

2.2 Description on the proposed approach

In this section, we present the key components of the proposed approach. Our approach uses the following neural networks:

- **Encoders $\boldsymbol{\mathcal{E}}\left(\boldsymbol{x}_0,\ \mathbf{p};\ \boldsymbol{\beta}\right)$ and $\boldsymbol{\mathcal{C}}\left(\boldsymbol{x}_0,\ \mathbf{p};\ \boldsymbol{\alpha}\right)$**: Note that both $\boldsymbol{\mathcal{E}}$ and $\boldsymbol{\mathcal{C}}$ are neural networks with parameters $\boldsymbol{\beta}$ and $\boldsymbol{\alpha}$ respectively. The network $\boldsymbol{\mathcal{E}}\left(.,.,\boldsymbol{\beta}\right) : \mathcal{G} \times \mathcal{X}_p \mapsto \mathbb{R}^m$ takes in $\boldsymbol{x}_0,\ \mathbf{p}$, as defined in (1), as inputs and outputs an m dimensional initial condition for the latent dynamical system given below:

$$diag\left(\frac{d\boldsymbol{y}}{d\boldsymbol{\tau}}\right) = \boldsymbol{\mathcal{C}}(\boldsymbol{x}_0, \mathbf{p};\ \boldsymbol{\alpha}), \qquad \boldsymbol{y}(\mathbf{0}) = \boldsymbol{\mathcal{E}}\left(\boldsymbol{x}_0, \mathbf{p};\ \boldsymbol{\beta}\right) = \boldsymbol{y}_0, \tag{2}$$

  where $\boldsymbol{y} \in \mathbb{R}^m$, $\boldsymbol{\tau} \in \mathbb{R}^m$ is a nonlinear transformation of time as described by a neural network below. The network $\boldsymbol{\mathcal{C}}\left(.,.,\boldsymbol{\alpha}\right) : \mathcal{G} \times \mathcal{X}_p \mapsto \mathbb{R}^m$ takes in $\boldsymbol{x}_0,\ \mathbf{p}$, as defined in (1), as inputs and outputs an m dimensional slope vector (constant velocity) for the latent dynamics as described in (2).
- **Nonlinear Time Transformation $\boldsymbol{\tau}\left(t,\ \boldsymbol{x}_0,\ \mathbf{p};\ \boldsymbol{\nu}\right)$**: In (2), $\boldsymbol{\tau}$ is a neural network with parameters $\boldsymbol{\nu}$. The network $\boldsymbol{\tau}\left(.,.,.;\boldsymbol{\nu}\right) : I \times \mathcal{G} \times \mathcal{X}_p \mapsto \mathbb{R}^m$ performs a nonlinear transformation on the time variable which "stretches/squeezes" time in the latent space, thereby allowing for varying levels of attention to different regions in the solution depending on the inputs $\boldsymbol{x}_0,\ \mathbf{p}$. Note that the solution of (2) is a sequence of linear trajectories.

$$\boldsymbol{y}\left(t,\ \boldsymbol{x}_0,\ \mathbf{p}\right) = \boldsymbol{\mathcal{E}}(\boldsymbol{x}_0, \mathbf{p};\ \boldsymbol{\beta}) + \boldsymbol{\tau}\left(t,\ \boldsymbol{x}_0,\ \mathbf{p};\ \boldsymbol{\nu}\right) \circ \boldsymbol{\mathcal{C}}(\boldsymbol{x}_0, \mathbf{p};\ \boldsymbol{\alpha}). \tag{3}$$

- **Decoder $\boldsymbol{\mathcal{D}}\left(\boldsymbol{y};\ \boldsymbol{\theta}\right)$** : The decoder network $\boldsymbol{\mathcal{D}}(.;\ \boldsymbol{\theta}) : \mathbb{R}^m \mapsto \mathbb{R}^{n_x}$ with parameters, $\boldsymbol{\theta}$, decodes the solution, $\boldsymbol{y}$, in (3), back to the solution of original dynamics, $\boldsymbol{x}$, in (1).

Based on the above networks, our procedure can be summarized as follows. For a given initial condition, $\boldsymbol{x}_0$, and parameters, $\mathbf{p}$, the encoders, $\boldsymbol{\mathcal{E}}$ and $\boldsymbol{\mathcal{C}}$ generate the initial condition and the constant velocity vector for the latent dynamics described in (2). The solution of this latent dynamics is given in (3). The decoder then retrieves the solution $\boldsymbol{x}(t)$ to the original dynamics (1). The networks are trained, in tandem, to find the optimal parameters $\boldsymbol{\alpha},\ \boldsymbol{\beta},\ \boldsymbol{\theta},\ \boldsymbol{\nu}$ that minimize the loss function (details in Appendix A.2) that compares the generated solution $\hat{\boldsymbol{x}}(t)$ to the true solution $\boldsymbol{x}(t)$.

The training data takes the form:

$$\{\{\boldsymbol{x}_0,\ \mathbf{p}\}_i,\ \{\boldsymbol{x}(t_0),\ \boldsymbol{x}(t_1), \ldots \boldsymbol{x}(t_M)\}_i\}_{i=1}^N, \tag{4}$$

where N is the total number of training sample trajectories, and $t_0, \dots t_M$ are the temporal collocation points for each trajectory, which are used to construct the loss function (see Appendix A.2 for more details).

It should be noted that our approach has some similarities with the methodology proposed by Sulzer and Buck in [22]. They were the first, to our knowledge, to propose a fully linear latent space. However, in their work [22], the authors do not consider a learned nonlinear transformation on the time variable, denoted by $\boldsymbol{\tau}$ in this work. Note that the proposed non-linear transformation of time is essential in proving the universal approximation results in theorem 1. Further, in section 3.6, we discuss the vital role the learned time transformation plays numerically in our approach for simulating StODEs.

In the below sections, we will derive the conditions under which our approach can approximate the solution of a nonlinear system of ODEs on a compact set to any degree of accuracy ε. To that end, let us consider the following definition:

Definition 2 *Class of functions $\mathcal{N}^{\phi}_{a,b,a+b+2}$* Let $\phi : \mathbb{R} \to \mathbb{R}$ be any non-affine, Lipschitz continuous function which is continuously differentiable at least at one point, having a nonzero derivative at that point. Then, $\mathcal{N}^{\phi}_{a,b,a+b+2}$ represents the class of functions described by feedforward neural networks with 'a' neurons in the input layer, 'b' neurons in the output layer, and an arbitrary number of hidden layers, each with '$a+b+2$' neurons and activation function ϕ. Every neuron in the output layer has the identity activation function.

Lemma 1 *Consider the autonomous ordinary differential equation in* (1)*. Assume the following:*

1. $\boldsymbol{f}_{\mathbf{p}}(\boldsymbol{x}(t))$ *is globally Lipschitz continuous*[2].
2. $\boldsymbol{f}_{\mathbf{p}}(\boldsymbol{x}(t))$ *is twice continuously differentiable with respect to both* $\boldsymbol{x}(t)$ *and* $\mathbf{p}$ *on* $\mathcal{G} \times \mathcal{X}_p$.

Then, the flow map in definition 1, $\boldsymbol{\psi}_{\boldsymbol{x}}(t,\ \boldsymbol{x}_0,\ \mathbf{p})$ *is twice continuously differentiable on* $\mathcal{W}$ *with* $I_{\boldsymbol{x}_0;\mathbf{p}} = \mathbb{R}$.

Proof: Rewriting the ODE (1) in terms of a new variable $\tilde{\boldsymbol{x}}(t)$ as:

$$\frac{d\tilde{\boldsymbol{x}}}{dt} = \tilde{\boldsymbol{f}}\left(\tilde{\boldsymbol{x}}(t)\right), \quad \tilde{\boldsymbol{x}}(t) = \begin{bmatrix} \boldsymbol{x}(t) \\ \mathbf{p} \end{bmatrix}, \quad \tilde{\boldsymbol{x}}(0) = \tilde{\boldsymbol{x}}_0 = \begin{bmatrix} \boldsymbol{x}_0 \\ \mathbf{p} \end{bmatrix}, \tag{5}$$

where

$$\tilde{\boldsymbol{f}}\left(\tilde{\boldsymbol{x}}(t)\right) = \begin{bmatrix} \boldsymbol{f}_{I_2\tilde{\boldsymbol{x}}(t)}\left(I_1\tilde{\boldsymbol{x}}(t)\right). \\ \mathbf{0} \end{bmatrix}$$

where, I_1 maps $\tilde{\boldsymbol{x}}(t)$ to $\boldsymbol{x}(t)$, and I_2 maps $\tilde{\boldsymbol{x}}(t)$ to $\mathbf{p}$. Since $\boldsymbol{f}_{\mathbf{p}}(\boldsymbol{x})$ is globally Lipschitz continuous, by the global existence theorem (Theorem B, Chapter 13 in [23]), we note that $\mathbb{R}$ is the interval of existence of the unique maximal solution of (5) for any given $\tilde{\boldsymbol{x}}_0$. Also note that $\tilde{f}$ is twice continuously differentiable on $\mathcal{P}$, where $\mathcal{P} = \mathcal{G} \times \mathcal{X}_p$, due to the assumption that $\boldsymbol{f}_{\mathbf{p}}(\boldsymbol{x}(t))$ is twice continuously differentiable with respect to both $\mathbf{p}$ and $\boldsymbol{x}(t)$. Now introduce the set:

$$\tilde{\mathcal{W}} = \bigcup_{\tilde{\boldsymbol{x}}_0 \in \mathcal{P}} \mathbb{R} \times \{\tilde{\boldsymbol{x}}_0\} \subseteq \mathbb{R} \times \mathcal{P},$$

and define the corresponding flow map for (5) as $\boldsymbol{\psi}_{\tilde{\boldsymbol{x}}} : \tilde{\mathcal{W}} \to \mathcal{P}$ such that $\boldsymbol{\psi}_{\tilde{\boldsymbol{x}}}(t, \tilde{\boldsymbol{x}}_0) = \tilde{\boldsymbol{x}}(t)$, where $\tilde{\boldsymbol{x}}(t)$ solves (5) for a given $\tilde{\boldsymbol{x}}_0$. Since $\tilde{f}$ is twice continuously differentiable on $\mathcal{P}$, by Theorem 6.1 in [24], we have $\boldsymbol{\psi}_{\tilde{\boldsymbol{x}}}(t, \tilde{\boldsymbol{x}}_0)$ is twice continuously differentiable on $\tilde{\mathcal{W}}$. Now, defining $\boldsymbol{\psi}_{\boldsymbol{x}}(t,\ \boldsymbol{x}_0,\ \mathbf{p}) = \boldsymbol{\psi}_{\tilde{\boldsymbol{x}}}(t, \tilde{\boldsymbol{x}_0})$ concludes the proof.

Theorem 1 *Consider the autonomous ordinary differential equation in* (1) *and assume the following:*

1. *The conditions in lemma 1 are satisfied.*
2. *Assume that the initial condition* $\boldsymbol{x}_0 \in \mathcal{G}_0 \subset \mathcal{G}$*, where* $\mathcal{G}_0$ *is a non-empty compact set.*
3. *Consider the set* $E = I \times \mathcal{G}_0 \times \mathcal{X}_p$*, where* $I = [0,\ t^u]$*, (*$t^u \in \mathbb{R}^+$*) is a closed and bounded interval such that the following condition is satisfied:*

$$\exists t_j^* \in \mathbb{R},\ \ s.t\ \ \left[\boldsymbol{\psi}_{\boldsymbol{x}}\left(t,\ \boldsymbol{x}_0, \mathbf{p}\right)\right]_j - \left[\boldsymbol{\psi}_{\boldsymbol{x}}\left(t_j^*,\ \boldsymbol{x}_0, \mathbf{p}\right)\right]_j + \left.\frac{\partial\left[\boldsymbol{\psi}_{\boldsymbol{x}}\right]_j}{\partial t}\right|_{t=t_j^*}(t_j^*) \neq 0,\ \forall\left(t,\ \boldsymbol{x}_0,\ \mathbf{p}\right) \in E,\ \forall j, \tag{6}$$

where $\left[\boldsymbol{\psi}_{\boldsymbol{x}}\left(t,\ \boldsymbol{x}_0, \mathbf{p}\right)\right]_j$ *denotes the* j^{th} *component of the flow map in definition 1.*

[2] $\boldsymbol{f}_{\mathbf{p}}(\boldsymbol{x})$ is globally Lipschitz continuous if there exists a non-negative constant M such that $\left\|\boldsymbol{f}_{\mathbf{p}_1}(\boldsymbol{x}_1) - \boldsymbol{f}_{\mathbf{p}_2}(\boldsymbol{x}_2)\right\|_2 \leq M\left\|\mathbf{r}_1 - \mathbf{r_2}\right\|_2, \forall \mathbf{r}_1, \mathbf{r}_2 \in \mathbb{R}^{n_x+n_p}$, where $\mathbf{r}_1 = [\boldsymbol{x}_1,\ \mathbf{p}_1]$ and $\mathbf{r}_2 = [\boldsymbol{x}_2,\ \mathbf{p}_2]$.

Then, $\forall m \geq n_x$, m being the latent dimension, and $\forall \varepsilon > 0$, there exists neural networks $\boldsymbol{\mathcal{E}}\left(.,.;\boldsymbol{\beta}\right) : \mathcal{G}_0 \times \mathcal{X}_p \mapsto \mathbb{R}^m$, $\boldsymbol{\mathcal{C}}\left(.,.;\boldsymbol{\alpha}\right) : \mathcal{G}_0 \times \mathcal{X}_p \mapsto \mathbb{R}^m$, $\boldsymbol{\mathcal{D}}(.;\ \boldsymbol{\theta}) : \mathbb{R}^m \mapsto \mathbb{R}^{n_x}$, and $\boldsymbol{\tau}\left(.,.,.;\boldsymbol{\nu}\right) : \mathbb{R} \times \mathcal{G}_0 \times \mathcal{X}_p \mapsto \mathbb{R}^m$ with the associated latent dynamics:

$$diag\left(\frac{d\boldsymbol{y}}{d\boldsymbol{\tau}}\right) = \boldsymbol{\mathcal{C}}(\boldsymbol{x}_0, \mathbf{p};\ \boldsymbol{\alpha}), \qquad \boldsymbol{y}(\mathbf{0}) = \boldsymbol{\mathcal{E}}\left(\boldsymbol{x}_0, \mathbf{p};\ \boldsymbol{\beta}\right) = \boldsymbol{y}_0, \tag{7}$$

such that:

$$\sup_{(t,\ \boldsymbol{x}_0,\ \mathbf{p}) \in E} \left(\left\|\boldsymbol{\psi}_{\boldsymbol{x}}\left(t,\ \boldsymbol{x}_0, \mathbf{p}\right) - \boldsymbol{\mathcal{D}}\left(\boldsymbol{\mathcal{E}}(\boldsymbol{x}_0, \mathbf{p};\ \boldsymbol{\beta}) + \boldsymbol{\tau}\left(t, \boldsymbol{x}_0, \mathbf{p};\ \boldsymbol{\nu}\right) \circ \boldsymbol{\mathcal{C}}(\boldsymbol{x}_0, \mathbf{p};\ \boldsymbol{\alpha});\ \boldsymbol{\theta}\right)\right\|_2\right) \leq \varepsilon,$$

where each network $\boldsymbol{\mathcal{E}}$, $\boldsymbol{\mathcal{C}}$, $\boldsymbol{\mathcal{D}}$, and $\boldsymbol{\tau}$ belong to the appropriate class of function defined in definition 2.

Proof: Note that the analytical solution for the constant velocity latent dynamics (7) can be written as:

$$\boldsymbol{y}(\boldsymbol{\tau}) = \boldsymbol{\mathcal{E}}(\boldsymbol{x}_0, \mathbf{p};\ \boldsymbol{\beta}) + \boldsymbol{\tau} \circ \boldsymbol{\mathcal{C}}(\boldsymbol{x}_0, \mathbf{p};\ \boldsymbol{\alpha}).$$

For any $(t, \boldsymbol{x}_0, \mathbf{p}) \in E$, define the error ρ as:

$$\rho = \left\|\boldsymbol{\psi}_{\boldsymbol{x}}\left(t,\ \boldsymbol{x}_0, \mathbf{p}\right) - \boldsymbol{\mathcal{D}}\left(\boldsymbol{\mathcal{E}}(\boldsymbol{x}_0, \mathbf{p};\ \boldsymbol{\beta}) + \boldsymbol{\tau} \circ \boldsymbol{\mathcal{C}}(\boldsymbol{x}_0, \mathbf{p};\ \boldsymbol{\alpha});\ \boldsymbol{\theta}\right)\right\|_2. \tag{8}$$

Now, note that $E \subset \mathcal{W}$, where E is compact and, from lemma 1, $\boldsymbol{\psi}_{\boldsymbol{x}}(t, \boldsymbol{x}_0,\ \mathbf{p})$ is continuous with respect to all variables on E. We will proceed by first showing that for the flow map $\boldsymbol{\psi}_{\boldsymbol{x}}\left(t,\ \boldsymbol{x}_0, \mathbf{p}\right)$, there exists $\boldsymbol{T} \in \mathbb{R}^{m \times n_x}$ with linearly independent columns ($m \geq n_x$), $\mathbf{g}\left(\boldsymbol{x}_0,\ \mathbf{p}\right) : \mathcal{G}_0 \times \mathcal{X}_p \mapsto \mathbb{R}^m$ continuous with respect to both arguments, $\boldsymbol{f}\left(\boldsymbol{x}_0,\ \mathbf{p}\right) : \mathcal{G}_0 \times \mathcal{X}_p \mapsto \mathbb{R}^m$ continuous with respect to both arguments, and $\boldsymbol{h}(t, \boldsymbol{x}_0, \mathbf{p}) : I \times \mathcal{G}_0 \times \mathcal{X}_p \mapsto \mathbb{R}^m$ continuous with respect to all arguments such that:

$$\boldsymbol{T}\left(\boldsymbol{\psi}_{\boldsymbol{x}}\left(t,\ \boldsymbol{x}_0, \mathbf{p}\right)\right) = \mathbf{g}(\boldsymbol{x}_0, \mathbf{p}) + \boldsymbol{h}(t, \boldsymbol{x}_0, \mathbf{p}) \circ \boldsymbol{f}(\boldsymbol{x}_0, \mathbf{p}). \tag{9}$$

Since $\boldsymbol{\psi}_{\boldsymbol{x}}\left(t,\ \boldsymbol{x}_0, \mathbf{p}\right)$ is continuously differentiable on $\mathcal{W}$ (lemma 1), one can apply Taylor's theorem [25] for each component $\left[\boldsymbol{\psi}_{\boldsymbol{x}}\left(t,\ \boldsymbol{x}_0, \mathbf{p}\right)\right]_i$ of the flow map ($i = 1, \ldots n_x$) around $t = t_i^*$, where $t_i^* \in \mathbb{R}$. We have:

$$\left[\boldsymbol{\psi}_{\boldsymbol{x}}\left(t,\ \boldsymbol{x}_0, \mathbf{p}\right)\right]_i = \left[\boldsymbol{\psi}_{\boldsymbol{x}}\left(t_i^*,\ \boldsymbol{x}_0, \mathbf{p}\right)\right]_i + \left.\frac{\partial\left[\boldsymbol{\psi}_{\boldsymbol{x}}\right]_i}{\partial t}\right|_{t=t_i^*}(t - t_i^*) + \left[\boldsymbol{u}(t,\ \boldsymbol{x}_0, \mathbf{p})\right]_i (t - t_i^*), \tag{10}$$

where $\lim_{t \to t_i^*}\left[\boldsymbol{u}(t, \boldsymbol{x}_0, \mathbf{p})\right]_i = 0$. Applying the linear transformation $\boldsymbol{T}$ on both sides of (10) we have the ith component as:

$$\sum_{j=1}^{n_x} \boldsymbol{T}_{ij}\left[\boldsymbol{\psi}_{\boldsymbol{x}}\left(t,\ \boldsymbol{x}_0, \mathbf{p}\right)\right]_j = \sum_{j=1}^{n_x}\left(\boldsymbol{T}_{ij}\left[\boldsymbol{\psi}_{\boldsymbol{x}}\left(t_j^*,\ \boldsymbol{x}_0, \mathbf{p}\right)\right]_j + \boldsymbol{T}_{ij}\left.\frac{\partial\left[\boldsymbol{\psi}_{\boldsymbol{x}}\right]_j}{\partial t}\right|_{t=t_j^*}(t - t_j^*) + \boldsymbol{T}_{ij}\left[\boldsymbol{u}(t,\ \boldsymbol{x}_0, \mathbf{p})\right]_j (t - t_j^*)\right), \tag{11}$$

Comparing (11) and (9), we have:

$$\left[\mathbf{g}(\boldsymbol{x}_0, \mathbf{p})\right]_i = \sum_{j=1}^{n_x} \boldsymbol{T}_{ij}\left[\boldsymbol{\psi}_{\boldsymbol{x}}\left(t_j^*,\ \boldsymbol{x}_0, \mathbf{p}\right)\right]_j - \sum_{j=1}^{n_x} \boldsymbol{T}_{ij}\left.\frac{\partial\left[\boldsymbol{\psi}_{\boldsymbol{x}}\right]_j}{\partial t}\right|_{t=t_j^*}(t_j^*),$$

where it is clear that $\mathbf{g}(\boldsymbol{x}_0, \mathbf{p})$ is continuous on $\mathcal{G}_0 \times \mathcal{X}_p$ since the flow map $\boldsymbol{\psi}_{\boldsymbol{x}}$ is continuously differentiable on $E \subset \mathcal{W}$ (lemma 1). Comparing (11) and (9), we also have:

$$\left[\boldsymbol{h}(t, \boldsymbol{x}_0, \mathbf{p})\right]_i \times \left[\boldsymbol{f}(\boldsymbol{x}_0, \mathbf{p})\right]_i = \sum_{j=1}^{n_x}\left(\boldsymbol{T}_{ij}\left.\frac{\partial\left[\boldsymbol{\psi}_{\boldsymbol{x}}\right]_j}{\partial t}\right|_{t=t_j^*}(t) + \boldsymbol{T}_{ij}\left[\boldsymbol{u}(t,\ \boldsymbol{x}_0, \mathbf{p})\right]_j t - \boldsymbol{T}_{ij}\left[\boldsymbol{u}(t,\ \boldsymbol{x}_0, \mathbf{p})\right]_j t_j^*\right), \tag{12}$$

Therefore,

$$\left[\boldsymbol{f}(\boldsymbol{x}_0, \mathbf{p})\right]_i = \frac{\sum_{j=1}^{n_x}\left(\boldsymbol{T}_{ij}\left.\frac{\partial\left[\boldsymbol{\psi}_{\boldsymbol{x}}\right]_j}{\partial t}\right|_{t=t_j^*}(t) + \boldsymbol{T}_{ij}\left[\boldsymbol{u}(t,\ \boldsymbol{x}_0, \mathbf{p})\right]_j t - \boldsymbol{T}_{ij}\left[\boldsymbol{u}(t,\ \boldsymbol{x}_0, \mathbf{p})\right]_j t_j^*\right)}{\left[\boldsymbol{h}(t, \boldsymbol{x}_0, \mathbf{p})\right]_i}, \quad \left[\boldsymbol{h}(t, \boldsymbol{x}_0, \mathbf{p})\right]_i \neq \mathbf{0}, \tag{13}$$

Now, since left-hand side of (13) is independent of time, the right hand side (R.H.S) should be independent of time as well. Considering the derivative of R.H.S w.r.t time and setting it to 0, we have the first order homogeneous linear differential equation for each component $[\boldsymbol{h}(t, \boldsymbol{x}_0, \mathbf{p})]_i$ as follows:

$$\frac{\partial \left[\boldsymbol{h}(t, \boldsymbol{x}_0, \mathbf{p})\right]_i}{\partial t} + q_i(t, \boldsymbol{x}_0, \mathbf{p}) \left[\boldsymbol{h}(t, \boldsymbol{x}_0, \mathbf{p})\right]_i = 0, \tag{14}$$

where

$$q_i(t, \boldsymbol{x}_0, \mathbf{p}) = -\frac{\sum_{j=1}^{n_x} \left(\boldsymbol{T}_{ij} \frac{\partial [\boldsymbol{\psi}_{\boldsymbol{x}}]_j}{\partial t}\Big|_{t=t_j^*} + \boldsymbol{T}_{ij} \left[\boldsymbol{u}(t,\ \boldsymbol{x}_0, \mathbf{p})\right]_j + t\boldsymbol{T}_{ij} \left[\boldsymbol{u}'(t,\ \boldsymbol{x}_0, \mathbf{p})\right]_j - t_j^* \boldsymbol{T}_{ij} \left[\boldsymbol{u}'(t,\ \boldsymbol{x}_0, \mathbf{p})\right]_j \right)}{\sum_{j=1}^{n_x} \left(\boldsymbol{T}_{ij} \frac{\partial [\boldsymbol{\psi}_{\boldsymbol{x}}]_j}{\partial t}\Big|_{t=t_j^*} (t) + \boldsymbol{T}_{ij} \left[\boldsymbol{u}(t,\ \boldsymbol{x}_0, \mathbf{p})\right]_j t - \boldsymbol{T}_{ij} \left[\boldsymbol{u}(t,\ \boldsymbol{x}_0, \mathbf{p})\right]_j t_j^* \right)}, \tag{15}$$

where $\boldsymbol{u}'$ denotes derivative with respect to time. The general solution to (14) can be written as:

$$\left[\boldsymbol{h}(t, \boldsymbol{x}_0, \mathbf{p})\right]_i = A \exp\left(Q_i(t, \boldsymbol{x}_0, \mathbf{p})\right), \tag{16}$$

where $Q_i(t, \boldsymbol{x}_0, \mathbf{p})$ is an antiderivative of $-q_i(t, \boldsymbol{x}_0, \mathbf{p})$. Now choose any arbitrary $A > 0$ such that $[\boldsymbol{h}(t, \boldsymbol{x}_0, \mathbf{p})]_i > 0$ and $[\boldsymbol{h}(t, \boldsymbol{x}_0, \mathbf{p})]_i \neq \mathbf{0}$, $\forall (t, \boldsymbol{x}_0, \mathbf{p}) \in E$ in (13). Note that $Q_i(t, \boldsymbol{x}_0, \mathbf{p})$ is continuous (and hence $[\boldsymbol{h}(t, \boldsymbol{x}_0, \mathbf{p})]_i$) on E if $q_i(t, \boldsymbol{x}_0, \mathbf{p})$ is continuous on E. Further, note that $q_i(t, \boldsymbol{x}_0, \mathbf{p})$ in (15) is continuous on E if $\boldsymbol{u}(t,\ \boldsymbol{x}_0, \mathbf{p})$ and $\boldsymbol{u}'(t,\ \boldsymbol{x}_0, \mathbf{p})$ are continuous on E and the denominator of (15) is non-zero $\forall\, (t,\ \boldsymbol{x}_0,\ \mathbf{p}) \in E$. Note that $\boldsymbol{u}(t,\ \boldsymbol{x}_0, \mathbf{p})$ and $\boldsymbol{u}'(t,\ \boldsymbol{x}_0, \mathbf{p})$ are continuous on E since the flow map $\boldsymbol{\psi}_{\boldsymbol{x}}$ is twice continuously differentiable on $E \subset \mathcal{W}$ (lemma 1). Now, using (10), the denominator of (15) can be rewritten as:

$$\sum_{j=1}^{n_x} \boldsymbol{T}_{ij} \left(\left[\boldsymbol{\psi}_{\boldsymbol{x}}\left(t,\ \boldsymbol{x}_0, \mathbf{p}\right)\right]_j - \left[\boldsymbol{\psi}_{\boldsymbol{x}}\left(t_j^*,\ \boldsymbol{x}_0, \mathbf{p}\right)\right]_j + \frac{\partial \left[\boldsymbol{\psi}_{\boldsymbol{x}}\right]_j}{\partial t}\Big|_{t=t_j^*} (t_j^*) \right).$$

Now, choose $\boldsymbol{T}$ such that in addition to having linearly independent columns, $\boldsymbol{T}$ also satisfy the property that, if all components of $\boldsymbol{x}$ are non-zero, then all components of $\boldsymbol{T}\boldsymbol{x}$ are non-zero as well. Such a $\boldsymbol{T}$ indeed exists. For instance, one such $\boldsymbol{T}$ can be formed by stacking identity matrices of size $n_x \times n_x$ one below the other. Therefore, by choosing such a $\boldsymbol{T}$, for the denominator (15) to be non-zero, it is sufficient that:

$$\exists t_j^* \in \mathbb{R},\ \ s.t\ \ \left[\boldsymbol{\psi}_{\boldsymbol{x}}\left(t,\ \boldsymbol{x}_0, \mathbf{p}\right)\right]_j - \left[\boldsymbol{\psi}_{\boldsymbol{x}}\left(t_j^*,\ \boldsymbol{x}_0, \mathbf{p}\right)\right]_j + \frac{\partial \left[\boldsymbol{\psi}_{\boldsymbol{x}}\right]_j}{\partial t}\Big|_{t=t_j^*} (t_j^*) \neq 0,\ \forall\, (t,\ \boldsymbol{x}_0,\ \mathbf{p}) \in E,\ \forall j \in \{1, \dots n_x\}, \tag{17}$$

which is satisfied by item 3 in the assumptions of the theorem. Therefore, the antiderivative $Q(t, \boldsymbol{x}_0, \mathbf{p})$ is continuous with respect to all arguments, leading to $[\boldsymbol{h}(t, \boldsymbol{x}_0, \mathbf{p})]_i$ being continuous with respect to all the arguments on E. Further, by substituting (16) back into (13), it is clear that $\boldsymbol{f}(\boldsymbol{x}_0, \mathbf{p})$ is also continuous with respect to both arguments on $\mathcal{G}_0 \times \mathcal{X}_p$ where we have used the assumption that $\boldsymbol{\psi}_{\boldsymbol{x}}$ is continuously differentiable on $E \subset \mathcal{W}$ (lemma 1).

Now multiplying both sides of (9) with $\boldsymbol{T}^\dagger$ (pseudo-inverse), we have:

$$\begin{aligned} \boldsymbol{T}^\dagger \boldsymbol{T} \left(\boldsymbol{\psi}_{\boldsymbol{x}}\left(t,\ \boldsymbol{x}_0, \mathbf{p}\right)\right) &= \boldsymbol{T}^\dagger \left(\mathbf{g}(\boldsymbol{x}_0, \mathbf{p}) + \boldsymbol{h}(t, \boldsymbol{x}_0, \mathbf{p}) \circ \boldsymbol{f}(\boldsymbol{x}_0, \mathbf{p})\right) \\ \implies \boldsymbol{\psi}_{\boldsymbol{x}}\left(t,\ \boldsymbol{x}_0, \mathbf{p}\right) &= \boldsymbol{T}^\dagger \left(\mathbf{g}(\boldsymbol{x}_0, \mathbf{p}) + \boldsymbol{h}(t, \boldsymbol{x}_0, \mathbf{p}) \circ \boldsymbol{f}(\boldsymbol{x}_0, \mathbf{p})\right), \end{aligned} \tag{18}$$

since we assumed that $\boldsymbol{T}$ has linearly independent columns. Also, note that one needs $m \geq n_x$ for $\boldsymbol{T}$ to have linearly independent columns. Now, using (18) the error (8) can be rewritten as:

$$\left\| \boldsymbol{T}^\dagger \left(\mathbf{g}(\boldsymbol{x}_0, \mathbf{p}) + \boldsymbol{h}(t, \boldsymbol{x}_0, \mathbf{p}) \circ \boldsymbol{f}(\boldsymbol{x}_0, \mathbf{p})\right) - \boldsymbol{\mathcal{D}}\left(\boldsymbol{\mathcal{E}}(\boldsymbol{x}_0, \mathbf{p};\ \boldsymbol{\beta}) + \boldsymbol{\tau} \circ \boldsymbol{\mathcal{C}}(\boldsymbol{x}_0, \mathbf{p};\ \boldsymbol{\alpha});\ \boldsymbol{\theta}\right) \right\|_2$$

Adding and subtracting term $\boldsymbol{\mathcal{D}}\left(\mathbf{g}(\boldsymbol{x}_0, \mathbf{p}) + \boldsymbol{h}(t, \boldsymbol{x}_0, \mathbf{p}) \circ \boldsymbol{f}(\boldsymbol{x}_0, \mathbf{p}); \boldsymbol{\theta}\right)$ above and applying a triangle inequality we have:

$$\begin{aligned} &\left\| \boldsymbol{T}^\dagger \left(\mathbf{g}(\boldsymbol{x}_0, \mathbf{p}) + \boldsymbol{h}(t, \boldsymbol{x}_0, \mathbf{p}) \circ \boldsymbol{f}(\boldsymbol{x}_0, \mathbf{p})\right) - \boldsymbol{\mathcal{D}}\left(\boldsymbol{\mathcal{E}}(\boldsymbol{x}_0, \mathbf{p};\ \boldsymbol{\beta}) + \boldsymbol{\tau} \circ \boldsymbol{\mathcal{C}}(\boldsymbol{x}_0, \mathbf{p};\ \boldsymbol{\alpha});\ \boldsymbol{\theta}\right) \right\|_2 \\ &\leq \underbrace{\left\| \boldsymbol{T}^\dagger \left(\mathbf{g}(\boldsymbol{x}_0, \mathbf{p}) + \boldsymbol{h}(t, \boldsymbol{x}_0, \mathbf{p}) \circ \boldsymbol{f}(\boldsymbol{x}_0, \mathbf{p})\right) - \boldsymbol{\mathcal{D}}\left(\mathbf{g}(\boldsymbol{x}_0, \mathbf{p}) + \boldsymbol{h}(t, \boldsymbol{x}_0, \mathbf{p}) \circ \boldsymbol{f}(\boldsymbol{x}_0, \mathbf{p}); \boldsymbol{\theta}\right) \right\|_2}_{III} \\ &+ \underbrace{\left\| \boldsymbol{\mathcal{D}}\left(\mathbf{g}(\boldsymbol{x}_0, \mathbf{p}) + \boldsymbol{h}(t, \boldsymbol{x}_0, \mathbf{p}) \circ \boldsymbol{f}(\boldsymbol{x}_0, \mathbf{p}); \boldsymbol{\theta}\right) - \boldsymbol{\mathcal{D}}\left(\boldsymbol{\mathcal{E}}(\boldsymbol{x}_0, \mathbf{p};\ \boldsymbol{\beta}) + \boldsymbol{\tau} \circ \boldsymbol{\mathcal{C}}(\boldsymbol{x}_0, \mathbf{p};\ \boldsymbol{\alpha});\ \boldsymbol{\theta}\right) \right\|_2}_{IV} \end{aligned} \tag{19}$$

Now let us consider term (III) in (19). Given $\boldsymbol{T}^{\dagger}$, and continuous functions $\mathbf{g},\ \boldsymbol{h},\ \boldsymbol{f}$, $\forall\varepsilon_2$ there exists a neural network $\boldsymbol{\mathcal{D}}\left(.;\boldsymbol{\theta}(\varepsilon_2)\right)\in\mathcal{N}^{\phi}_{m,n_x,k}$ with parameters $\boldsymbol{\theta}(\varepsilon_2)$ such that, by the universal approximation theorem [21],

$$\sup_{(t,\ \boldsymbol{x}_0,\ \mathbf{p})\in E}\left\|\boldsymbol{T}^{\dagger}\left(\mathbf{g}(\boldsymbol{x}_0,\mathbf{p})+\boldsymbol{h}(t,\boldsymbol{x}_0,\mathbf{p})\circ\boldsymbol{f}(\boldsymbol{x}_0,\mathbf{p})\right)-\boldsymbol{\mathcal{D}}\left(\mathbf{g}(\boldsymbol{x}_0,\mathbf{p})+\boldsymbol{h}(t,\boldsymbol{x}_0,\mathbf{p})\circ\boldsymbol{f}(\boldsymbol{x}_0,\mathbf{p});\boldsymbol{\theta}(\varepsilon_2)\right)\right\|_2\leq\varepsilon_2, \quad (20)$$

Now let us consider the term (IV) in (19). We have:

$$\begin{aligned}&\left\|\boldsymbol{\mathcal{D}}\left(\mathbf{g}(\boldsymbol{x}_0,\mathbf{p})+\boldsymbol{h}(t,\boldsymbol{x}_0,\mathbf{p})\circ\boldsymbol{f}(\boldsymbol{x}_0,\mathbf{p});\boldsymbol{\theta}\right)-\boldsymbol{\mathcal{D}}\left(\boldsymbol{\mathcal{E}}(\boldsymbol{x}_0,\mathbf{p};\ \boldsymbol{\beta})+\boldsymbol{\tau}\circ\boldsymbol{\mathcal{C}}(\boldsymbol{x}_0,\mathbf{p};\ \boldsymbol{\alpha});\ \boldsymbol{\theta}\right)\right\|_2\\&\leq L\left(\underbrace{\left\|\mathbf{g}(\boldsymbol{x}_0,\mathbf{p})+\boldsymbol{h}(t,\boldsymbol{x}_0,\mathbf{p})\circ\boldsymbol{f}(\boldsymbol{x}_0,\mathbf{p})-\boldsymbol{\mathcal{E}}(\boldsymbol{x}_0,\mathbf{p};\ \boldsymbol{\beta})+\boldsymbol{\tau}\circ\boldsymbol{\mathcal{C}}(\boldsymbol{x}_0,\mathbf{p},\ \boldsymbol{\alpha})\right\|_2}_{V}\right)\end{aligned} \quad (21)$$

where we have used the fact that $\boldsymbol{\mathcal{D}}\left(.;\boldsymbol{\theta}\right)\in\mathcal{N}^{\phi}_{m,n_x,k}$ is Lipschitz continuous, with Lipschitz constant L, with respect to first argument, due to employing a Lipschitz continuous activation function. Now analyzing the term (V) in (21) leads to:

$$\begin{aligned}&\left\|\mathbf{g}(\boldsymbol{x}_0,\mathbf{p})+\boldsymbol{h}(t,\boldsymbol{x}_0,\mathbf{p})\circ\boldsymbol{f}(\boldsymbol{x}_0,\mathbf{p})-\boldsymbol{\mathcal{E}}(\boldsymbol{x}_0,\mathbf{p};\ \boldsymbol{\beta})+\boldsymbol{\tau}\circ\boldsymbol{\mathcal{C}}(\boldsymbol{x}_0,\mathbf{p},\ \boldsymbol{\alpha})\right\|_2\\&\leq\underbrace{\left\|\mathbf{g}(\boldsymbol{x}_0,\mathbf{p})-\boldsymbol{\mathcal{E}}(\boldsymbol{x}_0,\mathbf{p};\boldsymbol{\beta})\right\|_2}_{VII}+\underbrace{\left\|\boldsymbol{h}(t,\boldsymbol{x}_0,\mathbf{p})\circ\boldsymbol{f}(\boldsymbol{x}_0,\mathbf{p})-\boldsymbol{\tau}\circ\boldsymbol{\mathcal{C}}(\boldsymbol{x}_0,\mathbf{p},\boldsymbol{\alpha})\right\|_2}_{VI},\end{aligned} \quad (22)$$

where we have applied a triangle inequality. Now, for term (VII) in (22), note that by the universal approximation theorem [21], we have $\forall\varepsilon_3$ there exists a neural network $\boldsymbol{\mathcal{E}}\left(\boldsymbol{x}_0,\ \mathbf{p}\ ;\boldsymbol{\beta}(\varepsilon_3)\right)\in\mathcal{N}^{\phi}_{n_x+n_p,m,k}$ with parameters $\boldsymbol{\beta}(\varepsilon_3)$ such that,

$$\sup_{(t,\ \boldsymbol{x}_0,\ \mathbf{p})\in E}\left\|\mathbf{g}(\boldsymbol{x}_0,\mathbf{p})-\boldsymbol{\mathcal{E}}\left(\boldsymbol{x}_0,\ \mathbf{p}\ ;\boldsymbol{\beta}(\varepsilon_3)\right)\right\|_2\leq\varepsilon_3. \quad (23)$$

Analyzing term (VI) in (22), we have:

$$\begin{aligned}&\left\|\boldsymbol{h}(t,\boldsymbol{x}_0,\mathbf{p})\circ\boldsymbol{f}(\boldsymbol{x}_0,\mathbf{p})-\boldsymbol{\tau}\circ\boldsymbol{\mathcal{C}}(\boldsymbol{x}_0,\mathbf{p},\boldsymbol{\alpha})\right\|_2\\&=\left\|\boldsymbol{h}(t,\boldsymbol{x}_0,\mathbf{p})\circ\boldsymbol{f}(\boldsymbol{x}_0,\mathbf{p})-\boldsymbol{\tau}\circ\boldsymbol{f}(\boldsymbol{x}_0,\mathbf{p})+\boldsymbol{\tau}\circ\boldsymbol{f}(\boldsymbol{x}_0,\mathbf{p})-\boldsymbol{\tau}\circ\boldsymbol{\mathcal{C}}(\boldsymbol{x}_0,\mathbf{p},\boldsymbol{\alpha})\right\|_2\\&\leq\left\|(\boldsymbol{h}(t,\boldsymbol{x}_0,\mathbf{p})-\boldsymbol{\tau})\circ\boldsymbol{f}(\boldsymbol{x}_0,\mathbf{p})\right\|_2+\left\|\boldsymbol{\tau}\circ(\boldsymbol{f}(\boldsymbol{x}_0,\mathbf{p})-\boldsymbol{\mathcal{C}}(\boldsymbol{x}_0,\mathbf{p},\boldsymbol{\alpha}))\right\|_2\\&\leq\left\|\mathbf{F}_f\left(\boldsymbol{x}_0,\ \mathbf{p}\right)(\boldsymbol{h}(t,\boldsymbol{x}_0,\mathbf{p})-\boldsymbol{\tau})\right\|_2+\left\|\mathbf{T}_\tau\left(t,\boldsymbol{x}_0,\mathbf{p}\right)(\boldsymbol{f}(\boldsymbol{x}_0,\mathbf{p})-\boldsymbol{\mathcal{C}}(\boldsymbol{x}_0,\mathbf{p},\boldsymbol{\alpha}))\right\|_2\\&\leq\left\|\mathbf{F}_f\left(\boldsymbol{x}_0,\ \mathbf{p}\right)\right\|_2\left\|\boldsymbol{h}(t,\boldsymbol{x}_0,\mathbf{p})-\boldsymbol{\tau}\right\|_2+\left\|\mathbf{T}_\tau\left(t,\boldsymbol{x}_0,\mathbf{p}\right)\right\|_2\left\|\boldsymbol{f}(\boldsymbol{x}_0,\mathbf{p})-\boldsymbol{\mathcal{C}}(\boldsymbol{x}_0,\mathbf{p},\boldsymbol{\alpha})\right\|_2\end{aligned} \quad (24)$$

where $\mathbf{F}_f\left(\boldsymbol{x}_0,\ \mathbf{p}\right)$ is the diagonal matrix whose components are $\boldsymbol{f}(\boldsymbol{x}_0,\mathbf{p})$ and $\mathbf{T}_\tau\left(t,\boldsymbol{x}_0,\mathbf{p}\right)$ is the diagonal matrix whose components are $\boldsymbol{\tau}\left(t,\boldsymbol{x}_0,\mathbf{p};\ \boldsymbol{\nu}\right)$. To bound the last two terms in (24), we rely on the following two results (universal approximation theorem [21]): $\forall\varepsilon_4$ there exists a neural network $\boldsymbol{\mathcal{C}}\left(\boldsymbol{x}_0,\ \mathbf{p};\boldsymbol{\alpha}(\varepsilon_4)\right)\in\mathcal{N}^{\phi}_{n_x+n_p,m,k}$ such that,

$$\sup_{(t,\ \boldsymbol{x}_0,\ \mathbf{p})\in E}\left\|\boldsymbol{f}(\boldsymbol{x}_0,\mathbf{p})-\boldsymbol{\mathcal{C}}\left(\boldsymbol{x}_0,\ \mathbf{p};\boldsymbol{\alpha}(\varepsilon_4)\right)\right\|_2\leq\varepsilon_4, \quad (25)$$

and $\forall\varepsilon_5$ there exists a neural network $\boldsymbol{\tau}\left(t,\ \boldsymbol{x}_0,\ \mathbf{p};\ \boldsymbol{\nu}(\varepsilon_5)\right)\in\mathcal{N}^{\phi}_{n_x+n_p+1,m,k}$ such that,

$$\sup_{(t,\ \boldsymbol{x}_0,\ \mathbf{p})\in E}\left\|\boldsymbol{h}(t,\boldsymbol{x}_0,\mathbf{p})-\boldsymbol{\tau}\left(t,\ \boldsymbol{x}_0,\ \mathbf{p};\ \boldsymbol{\nu}(\varepsilon_5)\right)\right\|_2\leq\varepsilon_5. \quad (26)$$

Using all the results (18), (19), (21), (22), (24) the error in (8) can now be bounded as follows:

$$\begin{aligned}&\left\|\boldsymbol{\psi}_{\boldsymbol{x}}\left(t,\ \boldsymbol{x}_0,\mathbf{p}\right)-\boldsymbol{\mathcal{D}}\left(\boldsymbol{\mathcal{E}}(\boldsymbol{x}_0,\mathbf{p};\ \boldsymbol{\beta})+\boldsymbol{\tau}\circ\boldsymbol{\mathcal{C}}(\boldsymbol{x}_0,\mathbf{p};\ \boldsymbol{\alpha});\ \boldsymbol{\theta}\right)\right\|_2.\\&\leq\left\|\boldsymbol{T}^{\dagger}\left(\mathbf{g}(\boldsymbol{x}_0,\mathbf{p})+\boldsymbol{h}(t,\boldsymbol{x}_0,\mathbf{p})\circ\boldsymbol{f}(\boldsymbol{x}_0,\mathbf{p})\right)-\boldsymbol{\mathcal{D}}\left(\mathbf{g}(\boldsymbol{x}_0,\mathbf{p})+\boldsymbol{h}(t,\boldsymbol{x}_0,\mathbf{p})\circ\boldsymbol{f}(\boldsymbol{x}_0,\mathbf{p});\boldsymbol{\theta}\right)\right\|_2\\&+L\left(\left\|\mathbf{g}(\boldsymbol{x}_0,\mathbf{p})-\boldsymbol{\mathcal{E}}(\boldsymbol{x}_0,\mathbf{p};\boldsymbol{\beta})\right\|_2+\left\|\mathbf{F}_f\left(\boldsymbol{x}_0,\ \mathbf{p}\right)\right\|_2\left\|\boldsymbol{h}(t,\boldsymbol{x}_0,\mathbf{p})-\boldsymbol{\tau}\right\|_2+\left\|\mathbf{T}_\tau\left(t,\boldsymbol{x}_0,\mathbf{p}\right)\right\|_2\left\|\boldsymbol{f}(\boldsymbol{x}_0,\mathbf{p})-\boldsymbol{\mathcal{C}}(\boldsymbol{x}_0,\mathbf{p};\boldsymbol{\alpha})\right\|_2\right)\\&\leq\sup_{(t,\ \boldsymbol{x}_0,\ \mathbf{p})\in E}\left\|\boldsymbol{T}^{\dagger}\left(\mathbf{g}(\boldsymbol{x}_0,\mathbf{p})+\boldsymbol{h}(t,\boldsymbol{x}_0,\mathbf{p})\circ\boldsymbol{f}(\boldsymbol{x}_0,\mathbf{p})\right)-\boldsymbol{\mathcal{D}}\left(\mathbf{g}(\boldsymbol{x}_0,\mathbf{p})+\boldsymbol{h}(t,\boldsymbol{x}_0,\mathbf{p})\circ\boldsymbol{f}(\boldsymbol{x}_0,\mathbf{p});\boldsymbol{\theta}\right)\right\|_2\\&+L\sup_{(t,\ \boldsymbol{x}_0,\ \mathbf{p})\in E}\left(\left\|\mathbf{g}(\boldsymbol{x}_0,\mathbf{p})-\boldsymbol{\mathcal{E}}(\boldsymbol{x}_0,\mathbf{p};\boldsymbol{\beta})\right\|_2+\left\|\mathbf{F}_f\left(\boldsymbol{x}_0,\ \mathbf{p}\right)\right\|_2\left\|\boldsymbol{h}(t,\boldsymbol{x}_0,\mathbf{p})-\boldsymbol{\tau}\right\|_2\right)\\&+L\sup_{(t,\ \boldsymbol{x}_0,\ \mathbf{p})\in E}\left(\left\|\mathbf{T}_\tau\left(t,\boldsymbol{x}_0,\mathbf{p}\right)\right\|_2\left\|\boldsymbol{f}(\boldsymbol{x}_0,\mathbf{p})-\boldsymbol{\mathcal{C}}(\boldsymbol{x}_0,\mathbf{p};\boldsymbol{\alpha})\right\|_2\right).\end{aligned} \quad (27)$$

Now, using the results (20), (23), (25) and (26), and setting $\boldsymbol{\tau} = \boldsymbol{\tau}\left(t,\ \boldsymbol{x}_0,\ \mathbf{p};\ \boldsymbol{\nu}(\varepsilon_5)\right)$, $\boldsymbol{\mathcal{C}}(\boldsymbol{x}_0, \mathbf{p}; \boldsymbol{\alpha}) = \boldsymbol{\mathcal{C}}(\boldsymbol{x}_0, \mathbf{p}; \boldsymbol{\alpha}(\varepsilon_4))$, $\boldsymbol{\mathcal{E}}\left(\boldsymbol{x}_0,\ \mathbf{p}\ ; \boldsymbol{\beta}\right) = \boldsymbol{\mathcal{E}}\left(\boldsymbol{x}_0,\ \mathbf{p}\ ; \boldsymbol{\beta}(\varepsilon_3)\right)$, $\boldsymbol{\mathcal{D}}\left(.; \boldsymbol{\theta}\right) = \boldsymbol{\mathcal{D}}\left(.; \boldsymbol{\theta}(\varepsilon_2)\right)$ we have the estimate for the error (8) as:

$$\rho \leq \varepsilon_2 + L\left(\varepsilon_3 + \varepsilon_5 \times \sup_{(t,\ \boldsymbol{x}_0,\ \mathbf{p}) \in E} \left\|\mathbf{F}_f\left(\boldsymbol{x}_0,\ \mathbf{p}\right)\right\|_2 + \varepsilon_4 \times \sup_{(t,\ \boldsymbol{x}_0,\ \mathbf{p}) \in E} \left\|\mathbf{T}_\tau\left(t, \boldsymbol{x}_0, \mathbf{p}\right)\right\|_2\right)$$

Now, by Weierstrauss extreme value theorem we have $\sup_{(t,\ \boldsymbol{x}_0,\ \mathbf{p}) \in E} \left\|\mathbf{F}_f\left(\boldsymbol{x}_0,\ \mathbf{p}\right)\right\|_2 = c_1$ and $\sup_{(t,\ \boldsymbol{x}_0,\ \mathbf{p}) \in E} \left\|\mathbf{T}_\tau\left(t, \boldsymbol{x}_0, \mathbf{p}\right)\right\|_2 = c_2$. Therefore, we have:

$$\rho \leq \varepsilon_2 + L\left(\varepsilon_3 + \varepsilon_5 \times c_1 + \varepsilon_4 \times c_2\right).$$

Now, set $\varepsilon_2 = \frac{\varepsilon}{4}$, $\varepsilon_3 = \frac{\varepsilon}{4L}$, $\varepsilon_4 = \frac{\varepsilon}{4Lc_2}$, $\varepsilon_5 = \frac{\varepsilon}{4Lc_1}$. This concludes the proof.

Remark 1 *Dependence of dimension, m, of latent space on the accuracy ε to be achieved*

Theorem 1 shows that our constant velocity latent dynamics approach can approximate the flow map, $\boldsymbol{\psi}_{\boldsymbol{x}}\left(t,\ \boldsymbol{x}_0, \mathbf{p}\right)$, on a compact set to any degree of accuracy, ε, as long as the dimension of the latent dynamics, m, is greater than or equal to the dimension, n_x, of the original dynamics (1). Further, the latent dimension, m, does not depend on the accuracy, ε, one aims to achieve.

Remark 2 *Relaxing item 1 in lemma 1* Note that item 1, requiring $\boldsymbol{f}_{\mathbf{p}}\left(\boldsymbol{x}(t)\right)$ to be globally Lipschitz, is only necessary to guarantee the existence of solution on the entire real line, for any $(\boldsymbol{x}_0,\ \mathbf{p}) \in \mathcal{G}_0 \times \mathcal{X}_p$. However, if it is known that the solution exists on some closed and bounded interval, $\tilde{I} = [0,\ \tilde{t}]$, for any $(\boldsymbol{x}_0,\ \mathbf{p}) \in \mathcal{G}_0 \times \mathcal{X}_p$, then the requirement for $\boldsymbol{f}_{\mathbf{p}}\left(\boldsymbol{x}(t)\right)$ to be globally Lipschitz can be relaxed, (i.e. not required at all!). In this case, the set, $E = I \times \mathcal{G}_0 \times \mathcal{X}_p$ in item 3, has to be constructed such that $I \subseteq \tilde{I}$, and $t_j^* \in \tilde{I}$ (instead of $\mathbb{R}$) in (6). With these changes, the result in theorem 1 still holds.

Remark 3 *Comments on item 3 in theorem 1*

Note that, in general, the flow map, $\boldsymbol{\psi}_{\boldsymbol{x}}\left(t,\ \boldsymbol{x}_0, \mathbf{p}\right)$, is not known beforehand to verify item 3 in theorem 1. Examining item 3, we see that one possibility for violating item 3 occurs when the set E contains a pair $(\boldsymbol{x}_0,\ \mathbf{p})$ for which the solution $\boldsymbol{x}(t)$ to (1) is constant in time. However, this scenario has no practical significance and one must avoid such points while constructing the compact set E. Further, note that as long as the set $Z = \{t_j^*\}$ containing the zero points of (6) (for all possible choice of $(t,\ \boldsymbol{x}_0,\ \mathbf{p}) \in E$) is not the entire real line, item 3 is never violated. The key here is to choose the set E and variables t_j^* such that item 3 is satisfied. With the availability of additional information on $\boldsymbol{f}_{\mathbf{p}}\left(\boldsymbol{x}(t)\right)$, it might be possible to simplify item 3. We consider such an example in Corollary 1, where we assume that the dynamical system does not return to its initial state in the interval I. Further, in Corollary 2, we will show how item 3 simplifies in the case of a linear, autonomous ODE, giving rise to conditions on the set $\mathcal{G}_0$ and $\mathcal{X}_p$ such that the result in theorem 1 holds. Note that a linear system of ODEs (1), where $\boldsymbol{f}\left(\boldsymbol{x}(t)\right)$ is given by (28), is considered stiff if all the eigenvalues of $\mathbf{A}$ are negative and the stiffness ratio is large [26]. We will assume this setup in Corollary 2.

Corollary 1 *Consider the autonomous ordinary differential equation in* (1) *and assume the following:*

1. *Assume that the initial condition $\boldsymbol{x}_0 \in \mathcal{G}_0 \subset \mathcal{G}$, where $\mathcal{G}_0$ is a non-empty compact set.*
2. *item 2 in lemma 1 is satisfied.*
3. *Choose the set $E = I \times \mathcal{G}_0 \times \mathcal{X}_p$ where $I = [\varepsilon_t,\ t^u]$, $t^u \in \mathbb{R}^+$, and ε_t is a small positive number such that:*
   - *(a) Solution to* (1) *exists on $[0,\ t^u]$ for any $(\boldsymbol{x}_0,\ \mathbf{p}) \in \mathcal{G}_0 \times \mathcal{X}_p$.*
   - *(b) The system does not return to its initial state (for each component) in the interval I. That is, $\forall \boldsymbol{x}_0,\ \mathbf{p} \in \mathcal{G}_0 \times \mathcal{X}_p$ one has the solution $\left[\boldsymbol{x}(t)\right]_j \neq \left[\boldsymbol{x}_0\right]_j,\ \forall t \in I,$ and $\forall j = \{1, \ldots n_x\}$, where $[.]_j$ denotes the jth component of the vector.*

Then, the universal approximation result in theorem 1 holds.

Proof: The proof follows from analyzing each condition in theorem 1. First, note that item 1 in lemma 1 is relaxed here due to the assumption that solution to (1) exists on the interval $[0,\ t^u]$ (see explanation in remark 2). Simplifying item 3 in theorem 1 by choosing $t_j^* = 0$ we get:

$$\left[\boldsymbol{\psi}_{\boldsymbol{x}}\left(t,\ \boldsymbol{x}_0, \mathbf{p}\right)\right]_j - \left[\boldsymbol{\psi}_{\boldsymbol{x}}\left(0,\ \boldsymbol{x}_0, \mathbf{p}\right)\right]_j = \left[\boldsymbol{\psi}_{\boldsymbol{x}}\left(t,\ \boldsymbol{x}_0, \mathbf{p}\right)\right]_j - \left[\boldsymbol{x}_0\right]_j \neq 0,\ \forall\left(t,\ \boldsymbol{x}_0,\ \mathbf{p}\right) \in E,\ \forall j,$$

which is satisfied by item 3b. This concludes the proof.

Corollary 2 *Consider the autonomous ordinary differential equation in* (1) *with:*

$$\boldsymbol{f}_{\mathbf{p}}\left(\boldsymbol{x}(t)\right)=\mathbf{A}\boldsymbol{x}(t)+\mathbf{B}\mathbf{p}. \tag{28}$$

Then, the result in theorem 1 holds if the following conditions are satisfied:

1. $\mathbf{A}$ *has linearly independent eigenvectors such that all the eigenvalues are negative (and non-zero).*
2. $\boldsymbol{x}_0 \in \mathcal{G}_0$ *(a non-empty, compact set) and* $\mathbf{p} \in \mathcal{X}_p$ *(a compact set) such that for each* $j = 1, 2, \ldots n_x$ *one has:*

$$\begin{aligned}&\mathbf{v}_j^k\left(\mathbf{g}_k\left(\mathbf{p}\right)+\lambda^{(k)}\mathbf{a}_k\left(\boldsymbol{x}_0\right)\right)\geq 0\;\forall k \;\text{ or }\; \mathbf{v}_j^k\left(\mathbf{g}_k\left(\mathbf{p}\right)+\lambda^{(k)}\mathbf{a}_k\left(\boldsymbol{x}_0\right)\right)\leq 0\;\;\forall k,\\ &\text{and }\; \mathbf{v}_j^k\left(\mathbf{g}_k\left(\mathbf{p}\right)+\lambda^{(k)}\mathbf{a}_k\left(\boldsymbol{x}_0\right)\right)\neq 0 \text{ for some k},\end{aligned} \tag{29}$$

where $\mathbf{g}\left(\mathbf{p}\right)=\mathbf{E}^{-1}\mathbf{B}\mathbf{p},\quad \mathbf{a}\left(\boldsymbol{x}_0\right)=\mathbf{E}^{-1}\boldsymbol{x}_0$, $\mathbf{E}=\left[\,\mathbf{v}^1,\;\mathbf{v}^2\;\ldots\mathbf{v}^{n_x}\right]$ *is the matrix containing the linearly independent eigenvectors of* $\mathbf{A}$*, and* $\{\lambda^{(i)},\;\mathbf{v}^i\}_{i=1}^{n_x}$ *are the eigenpairs of* $\mathbf{A}$*.*

Proof: The proof involves checking the conditions in Theorem 1. Note that it is easy to verify that $\boldsymbol{f}_{\mathbf{p}}\left(\boldsymbol{x}(t)\right)$, given by (28), is globally Lipschitz continuous and twice continuously differentiable with respect to both $\boldsymbol{x}(t)$ and $\mathbf{p}$ (refer lemma 1 for the definition of globally Lipschitz continuous function). Defining the vectors $\mathbf{r}_1=[\boldsymbol{x}_1,\;\mathbf{p}_1]$ and $\mathbf{r}_2=[\boldsymbol{x}_2,\;\mathbf{p}_2]$ and the matrix $\mathbf{L}=[\mathbf{A},\;\mathbf{B}]$ we have:

$$\left\|\boldsymbol{f}_{\mathbf{p}_1}(\boldsymbol{x}_1)-\boldsymbol{f}_{\mathbf{p}_2}(\boldsymbol{x}_2)\right\|_2=\left\|\mathbf{L}\mathbf{r}_1-\mathbf{L}\mathbf{r}_2\right\|_2\leq\left\|\mathbf{L}\right\|_2\left\|\mathbf{r}_1-\mathbf{r}_2\right\|_2,\;\;\forall\mathbf{r}_1,\mathbf{r}_2\in\mathbb{R}^{n_x+n_p},$$

thereby satisfying condition 1 in theorem 1.

To verify condition 3, let us define $\mathbf{E}=\left[\,\mathbf{v}^1,\;\mathbf{v}^2\;\ldots\mathbf{v}^{n_x}\right]$ as the matrix containing the linearly independent eigenvectors of $\mathbf{A}$ and $\{\lambda^{(i)},\;\mathbf{v}^i\}_{i=1}^{n_x}$ as the eigenpairs of $\mathbf{A}$. Define:

$$\mathbf{g}\left(\mathbf{p}\right)=\mathbf{E}^{-1}\mathbf{B}\mathbf{p},\quad \mathbf{a}\left(\boldsymbol{x}_0\right)=\mathbf{E}^{-1}\boldsymbol{x}_0.$$

Then, based on the general solution of a linear non-homogeneous system of ODEs [27], we have:

$$\boldsymbol{\psi}_{\boldsymbol{x}}\left(t,\;\boldsymbol{x}_0,\mathbf{p}\right)=\sum_{k=1}^{n_x}\mathbf{v}^k\left(e^{\lambda^{(k)}t}\mathbf{g}_k\left(\mathbf{p}\right)\frac{\left(1-e^{-\lambda^{(k)}t}\right)}{\lambda^{(k)}}+\mathbf{a}_k\left(\boldsymbol{x}_0\right)e^{\lambda^{(k)}t}\right), \tag{30}$$

where $\mathbf{g}_k\left(\mathbf{p}\right)$ denotes the kth component of the vector. Evaluating the constraint in condition 3 for the flow map (30) we have:

$$\begin{aligned}&\left[\boldsymbol{\psi}_{\boldsymbol{x}}\left(t,\;\boldsymbol{x}_0,\mathbf{p}\right)\right]_j-\left[\boldsymbol{\psi}_{\boldsymbol{x}}\left(t_j^*,\;\boldsymbol{x}_0,\mathbf{p}\right)\right]_j+\left.\frac{\partial\left[\boldsymbol{\psi}_{\boldsymbol{x}}\right]_j}{\partial t}\right|_{t=t_j^*}\left(t_j^*\right)\\ &=\sum_{k=1}^{n_x}\mathbf{v}_j^k\left(\frac{\mathbf{g}_k\left(\mathbf{p}\right)}{\lambda^{(k)}}+\mathbf{a}_k\left(\boldsymbol{x}_0\right)\right)\left(e^{\lambda^{(k)}t}-e^{\lambda^{(k)}t_j^*}\right)+t_j^*e^{\lambda^{(k)}t_j^*}\mathbf{v}_j^k\left(\mathbf{g}_k\left(\mathbf{p}\right)+\lambda^{(k)}\mathbf{a}_k\left(\boldsymbol{x}_0\right)\right)\\ &=\sum_{k=1}^{n_x}\mathbf{v}_j^k\left(t_j^*e^{\lambda^{(k)}t_j^*}+\frac{\left(e^{\lambda^{(k)}t}-e^{\lambda^{(k)}t_j^*}\right)}{\lambda^{(k)}}\right)\left(\mathbf{g}_k\left(\mathbf{p}\right)+\lambda^{(k)}\mathbf{a}_k\left(\boldsymbol{x}_0\right)\right),\end{aligned} \tag{31}$$

where $\left[\boldsymbol{\psi}_{\boldsymbol{x}}\left(t,\;\boldsymbol{x}_0,\mathbf{p}\right)\right]_j$ denotes the jth component of the flow map as defined in condition 3. Therefore, condition 3 translates to:

$$\exists t_j^*\in\mathbb{R},\;\;s.t\sum_{k=1}^{n_x}\mathbf{v}_j^k\left(t_j^*e^{\lambda^{(k)}t_j^*}+\frac{\left(e^{\lambda^{(k)}t}-e^{\lambda^{(k)}t_j^*}\right)}{\lambda^{(k)}}\right)\left(\mathbf{g}_k\left(\mathbf{p}\right)+\lambda^{(k)}\mathbf{a}_k\left(\boldsymbol{x}_0\right)\right)\neq 0,\forall\left(t,\;\boldsymbol{x}_0,\;\mathbf{p}\right)\in E,\;\forall j, \tag{32}$$

Now assume that for $j=1,2,\ldots n_x$:

$$\begin{aligned}&\mathbf{v}_j^k\left(\mathbf{g}_k\left(\mathbf{p}\right)+\lambda^{(k)}\mathbf{a}_k\left(\boldsymbol{x}_0\right)\right)\geq 0\;\forall k \;\text{ or }\; \mathbf{v}_j^k\left(\mathbf{g}_k\left(\mathbf{p}\right)+\lambda^{(k)}\mathbf{a}_k\left(\boldsymbol{x}_0\right)\right)\leq 0\;\;\forall k,\\ &\text{and }\; \mathbf{v}_j^k\left(\mathbf{g}_k\left(\mathbf{p}\right)+\lambda^{(k)}\mathbf{a}_k\left(\boldsymbol{x}_0\right)\right)\neq 0 \text{ for some k}.\end{aligned} \tag{33}$$

If $\mathbf{v}_j^k \left(\mathbf{g}_k\left(\mathbf{p}\right) + \lambda^{(k)}\mathbf{a}_k\left(\boldsymbol{x}_0\right)\right) \geq 0\ \forall k$, then the constraint (32) can be satisfied if $\exists t_j^* \in \mathbb{R}$ such that $\forall t \in [0,\ t^u]$:

$$\left(t_j^* e^{\lambda^{(k)} t_j^*} + \frac{\left(e^{\lambda^{(k)} t} - e^{\lambda^{(k)} t_j^*}\right)}{\lambda^{(k)}}\right) > 0.$$

Since $\lambda^{(k)} < 0$, by choosing $t_j^* > t^u$ the above inequality is satisfied $\forall t \in [0,\ t^u]$. The explanation is similar for the case when $\mathbf{v}_j^k \left(\mathbf{g}_k\left(\mathbf{p}\right) + \lambda^{(k)}\mathbf{a}_k\left(\boldsymbol{x}_0\right)\right) \leq 0\ \forall k$. This concludes the proof.

Remark 4 *Note that item 2, in Corollary 2, gives a system of linear inequalities involving $\boldsymbol{x}_0$ and $\mathbf{p}$ which can be used to construct the set $\mathcal{G}_0$ and $\mathcal{X}_p$ based on the feasible region (if it exists) such that the result in theorem 1 holds.*

2.3 Architectural Variants

This section presents a few variants of the approach presented in section 2.2. There are several, simple modifications that can be made to create "stacked" variants of the architecture, similar to the DeepONet implementation in [15]. We tested the following four variants:

1. The "Full learning" approach: This approach is exactly the same as the one described in section 2.2. In this approach we have three encoders, $(\boldsymbol{\mathcal{E}},\ \boldsymbol{C},\ \boldsymbol{\tau})$, and one decoder, $\boldsymbol{\mathcal{D}}$. The description of each network is provided in section 2.2. A schematic of the approach is provided in figure 2.
2. The "Independent learning" approach: In this case, we have n_x triples of encoders, $(\boldsymbol{\mathcal{E}}_i,\ \boldsymbol{C}_i,\ \boldsymbol{\tau}_i)$, where each triple encodes to a unique set of latent dynamics. Additionally, there are separate decoders, $\boldsymbol{\mathcal{D}}_i$, for each ith latent dynamics, which recovers the associated i^{th} component of the solution vector $\boldsymbol{x}(t)$ in (1). A schematic of the approach is provided in figure 3.
3. The "Common encoder learning" approach: In this case, we have three encoders, $(\boldsymbol{\mathcal{E}},\ \boldsymbol{C},\ \boldsymbol{\tau})$, as described in section 2.2. However, we have n_x separate decoders, $\boldsymbol{\mathcal{D}}_i$, which decode the same latent dynamics to recover the associated i^{th} component of the solution vector $\boldsymbol{x}(t)$ in (1). A schematic of the approach is provided in figure 4.
4. The "Common decoder learning" approach: In this case, we have n_x triples of encoders, $(\boldsymbol{\mathcal{E}}_i,\ \boldsymbol{C}_i,\ \boldsymbol{\tau}_i)$, where each triple encodes to a unique set of latent dynamics. However, we have a single decoder, $\boldsymbol{\mathcal{D}}$, which separately decodes each ith latent dynamics to recover the associated i^{th} component of the solution vector $\boldsymbol{x}(t)$ in (1). A schematic of the approach is provided in figure 5.

Figure 6 shows the average point-wise relative error (49) (for a test data set), on the collisional-radiative charge state model section 3.2, achieved by each approach presented above. Each approach was tested with approximately the same number of trainable parameters. It is clear from figure 6 that the "independent learning" approach shows the best performance, for the given problem. For all the ODE numerical results (sections 3.1, 3.2), we only present results for the "independent learning" approach, while for the PDE problems (sections 3.3, 3.4), we present results for the "full" approach.

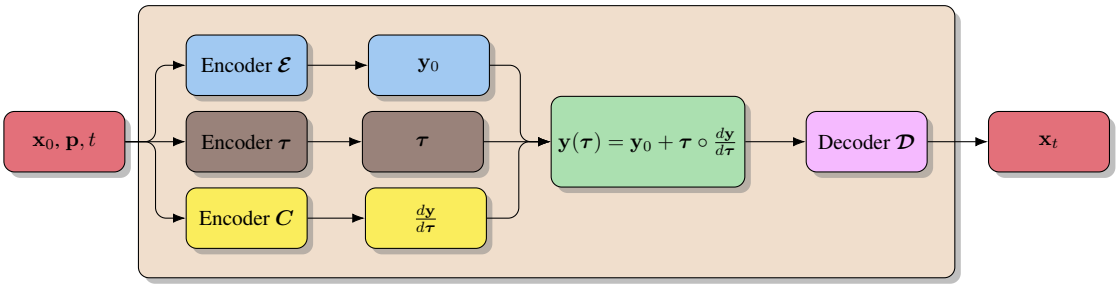

Figure 2: Schematic of the full learning approach.

3 Numerical Experiments

In this section, we numerically demonstrate the effectiveness of our proposed approach on a variety of prototype problems such as:

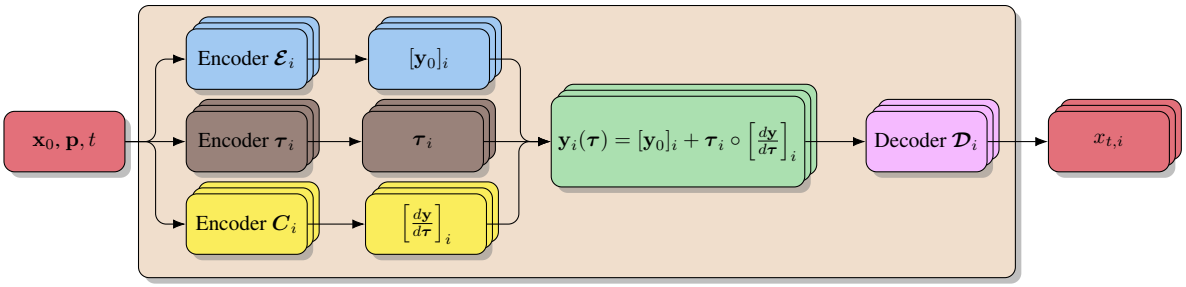

Figure 3: Schematic of independent learning approach.

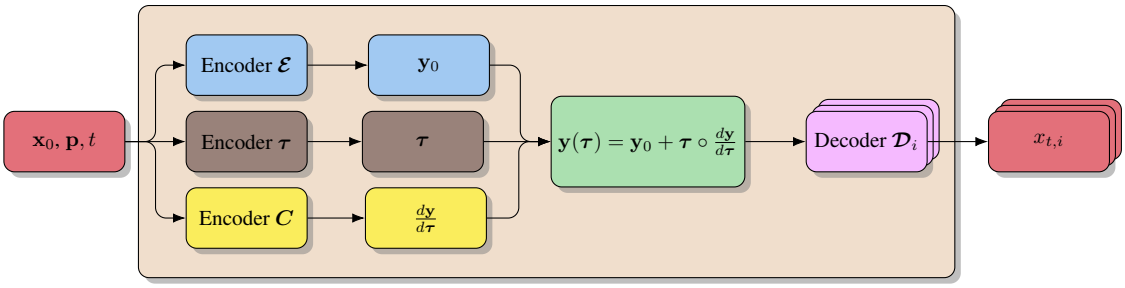

Figure 4: Schematic of common encoder learning approach: Note the single triple of encoder networks which map the initial conditions and parameters to the latent dynamics and n_x decoder networks which map from the latent space to the predicted solution.

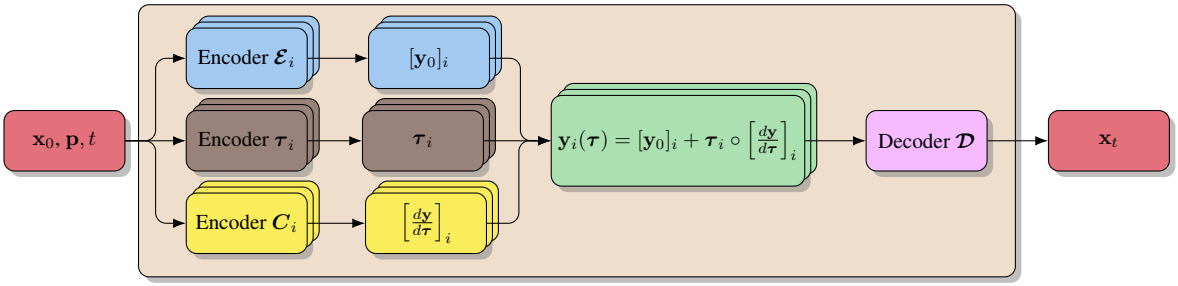

Figure 5: Schematic of common decoder learning approach: Note the n_x triples of encoder networks which map the initial conditions and parameters to the latent dynamics and single decoder network which maps from the latent space to the solution.

1. ROBER Stiff Chemical Kinetics Model [1]
2. Plasma Collisional-Radiative Model [2]
3. Allen-Cahn Phase Separation PDE [3]
4. Cahn-Hilliard Phase Separation PDE [3]

General experimental settings for all the problems and descriptions of methods adopted for comparison are detailed in Appendix A.

3.1 ROBER Stiff Chemical Kinetics Model

The ROBER chemical kinetics problem is a prototype stiff system of ODEs that describes the concentration of three species of reactants in a chemical reaction [1]. The model has been widely has been used to evaluate the performance of

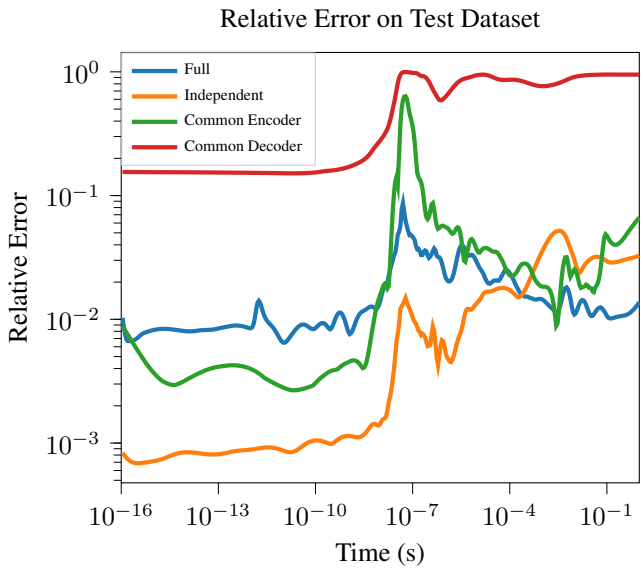

Figure 6: Average point-wise relative error (49), achieved by different approaches presented in section 2.3, for the full CR model (section 3.2) on the test dataset.

stiff integrators in traditional numerical analysis. The system is characterized by the following system of ODEs:

$$\begin{aligned} \frac{dx_1}{dt} &= -p_1 x_1 + p_3 x_2 x_3, \\ \frac{dx_2}{dt} &= p_1 x_1 - p_3 x_2 x_3 - p_2 x_2^2, \\ \frac{dx_3}{dt} &= p_2 x_2^2, \end{aligned} \tag{34}$$

where the second species, x_2, is the fastest evolving component, whereas the species x_1 and x_3 evolve slowly in comparison. This leads to numerical stiffness and difficulties in integration by explicit numerical solvers. In (34), the three reaction rates are typically chosen as $p_1 = 4 \cdot 10^{-2}$, $p_2 = 3 \cdot 10^{7}$, and $p_3 = 10^{4}$. Note that in (1), we have the parameters of the StODE as $\mathbf{p} = [p_1,\ p_2,\ p_3]$ and states $\boldsymbol{x} = [x_1,\ x_2,\ x_3]$.

3.1.1 Data Generation

For a given initial condition, $\boldsymbol{x}_0$, and parameters, $\mathbf{p}$, we integrate the system (34) with the Kvaerno5 stiff solver [28], from the Diffrax library [29], on a 50 point (i.e. $M = 50$ in (4)) logarithmically scaled time grid, spanning from $t = 10^{-5}s$ to $t = 10^{5}s$. In this problem, the initial condition is fixed consistently as $\boldsymbol{x}_0 = [1, 0, 0]$ and only the reaction rates, $\mathbf{p}$, vary across training samples. Similar to the data generation approach in [1], training input samples $(p_1,\ p_2,\ p_3)$ were sampled from $[0.2 \cdot 10^{-2}, 0.6 \cdot 10^{-2}] \times [1.5 \cdot 10^{7}, 3.5 \cdot 10^{7}] \times [5 \cdot 10^{3},\ 1.5 \cdot 10^{4}]$. The parameters of the training set, $(p_1,\ p_2,\ p_3)$, were sampled considering 16 linearly spaced collocation points in each domain. Thus, we consider a total of 4096 training samples. An additional 512 validation samples and 1000 test samples were generated using different collocation points.

3.1.2 Results

Our proposed approach was tested and compared with the Neural ODE [10] and DeepONet [15] approaches. Figure 7 shows a comparison of the average point-wise relative error, calculated via (49), for each method when applied to the test dataset. From figure 7, it is clear that our proposed method outperforms DeepONet by approximately one order of magnitude throughout the time series, while outperforming Neural ODE by several orders of magnitude. The computation is done using single precision floats, which means the error is close to machine precision for prediction on the early steps of the time series. The average error achieved by different machine learning methods has been tabulated in table 1. Further, figure 8 depicts a simulated trajectory for the proposed approach for a particular set of parameters, $\mathbf{p}$, from the test dataset, where we clearly see that the predicted solution matches closely to the one calculated by the numerical StODE solver. Additional results on the speedup achieved over the chosen traditional numerical solver (Kvaerno5 stiff solver) have been tabulated in table 2.

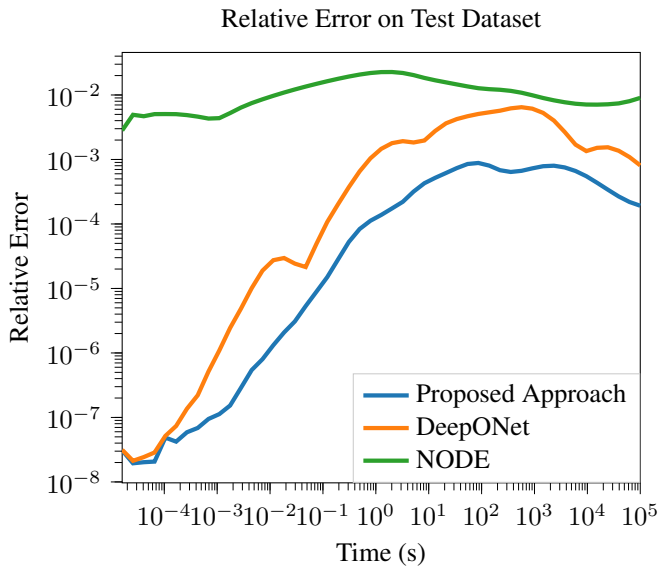

Figure 7: Average point-wise relative error over time (49) when evaluating ROBER chemical kinetics model on test data.

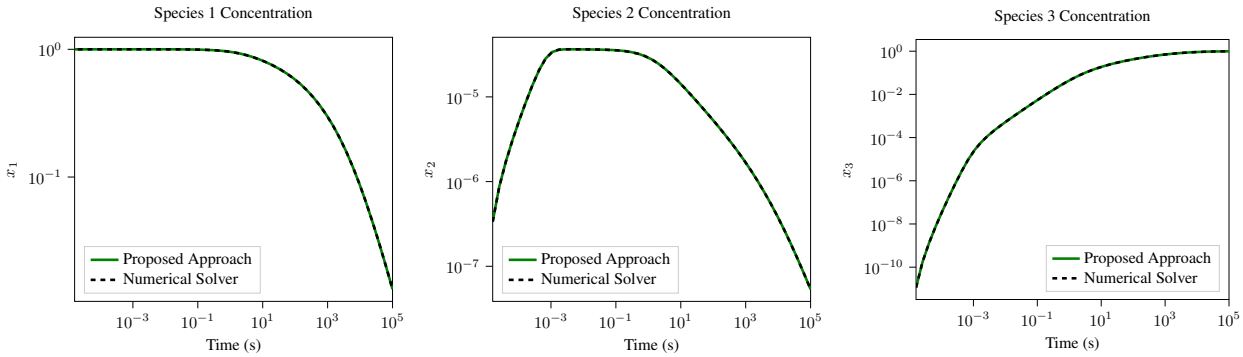

Figure 8: Simulated trajectory using the proposed approach for a particular set of parameters $\mathbf{p}$. Left to Right: Evolution of species x_1 with time; Evolution of species x_2 with time; Evolution of species x_3 with time.

3.2 Plasma Collisional-Radiative Model

In this section, we consider a collisional-radiative (CR) model, for a lithium plasma, which has more significant multiscale behavior, in comparison to the ROBER problem, in addition to being stiff. The CR model is a highly stiff, nonlinear dynamical system written as follows:

$$\frac{d\mathbf{N}}{dt} = \mathbf{R}(\mathbf{N}) \cdot \mathbf{N}, \quad \mathbf{N}(0) = \mathbf{N}_{initial}. \tag{35}$$

In the above equation, $\mathbf{N} \in \mathbb{R}^{n_x}$ and $\mathbf{R}$ is the $n_x \times n_x$ rate matrix with nonlinear dependence on $\mathbf{N}$. The rate matrix contains a set of rules for the up-transitions and down-transitions of electrons between the n_x discrete excited state levels of the state vector, $\mathbf{N}$. The rate matrix explicitly depends on the temperature, T_e, and the electron density, n_e. The dependence on temperature comes from the fact that the electron distribution is assumed to be a Maxwellian distribution, parameterized by T_e [30]. The electron density is defined as

$$n_e = \sum_{j=0}^{Z} j n_j, \tag{36}$$

where Z denotes the atomic number of the plasma element (in our simulation we consider Lithium, for which $Z = 3$), j is the ion charge state, and n_j is the lithium ion density at charge state j given by (37) [30]. We choose $L = 31$ in

(37), implying that $\mathbf{N} \in \mathbb{R}^{94}$, (i.e. there are 94 discrete excited states).

$$n_0 = \sum_{i=0}^{L-1} \mathbf{N}_i, \quad n_1 = \sum_{i=L}^{2L-1} \mathbf{N}_i, \quad n_2 = \sum_{i=2L}^{3L-1} \mathbf{N}_i, \quad n_3 = \mathbf{N}_{3L}. \tag{37}$$

The traditional approach to solving (35) are methods well suited for stiff problems, such as Backward Differentiation Formula (BDF) methods, described in detail in [31]. These approaches are implicit linear multistep methods and require solving a system of n_x equations at each time step. Solving this system becomes very expensive when n_x is large, as is the case for CR models with high-Z element impurities or when L is chosen to be large.

3.2.1 Data Generation

For data generation, (35) is integrated using the six-step BDF formula on a 400-step (i.e. $M = 400$ in (4)) logarithmic time grid on $t \in [1^{-16}, 1^{0}]$. We generate different initial conditions $\mathbf{N}_{initial}$ for (35) through two parameters n_A and n_{per} as follows:

$$\begin{aligned} &(\mathbf{N}_{initial})_0 = \left(1 - n_{per} - 92 \cdot 10^{-5} \cdot n_{per}\right) \cdot n_A, \\ &(\mathbf{N}_{initial})_1, (\mathbf{N}_{initial})_2, \ldots (\mathbf{N}_{initial})_{92} = 10^{-5} \cdot n_{per} \cdot n_A, \\ &(\mathbf{N}_{initial})_{93} = n_{per} \cdot n_A, \end{aligned} \tag{38}$$

where $(\mathbf{N}_{initial})_i$ denotes the ith component of $\mathbf{N}_{initial}$. We sample $(n_A,\ n_{per},\ T_e)$ from $[10^{14}, 10^{15}] \times [1 \cdot 10^{-3}, 2 \cdot 10^{-3}] \times [5,\ 95]$ to generate the training data, where n_A is the total number of lithium ions, of all charge states, in the plasma, T_e is the temperature in KeV, and n_{per} is a constant used to parameterize the initial electron distribution. Note that the sum of the entries in $\mathbf{N}_{initial}$ will be n_A. In fact, the total number of electrons is conserved for all time steps of the simulation. Further, note that in (1), we have the parameters $\mathbf{p} = [T_e,\ n_A]$ and $\boldsymbol{x}_0 = (\mathbf{N}_{initial}) = \mathcal{F}(\mathbf{n_p})$, where $\mathbf{n_p} = [n_A,\ n_{per}]$ and $\mathcal{F}$ is a map determined by (38). In implementation, our approach only acts on the the variables n_A, T_e, n_{per}, and t, the time variable, and learning the parameterization (38) becomes part of the learning task. The parameters of the training set, $(n_A,\ n_{per},\ T_e)$, were sampled considering 25 linearly spaced collocation points in each domain, leading to a total of 15625 samples. An additional 1000 validation samples and 4096 test samples were generated using different collocation points.

3.2.2 Results

We demonstrate our approach on two cases:

1. CR charge state model: The aim here is to predict only the four charge states $n_0, \ldots, n_3$ in (37).
2. Full CR model: The aim here is to predict the full state $\mathbf{N} \in \mathbb{R}^{94}$ in (35).

Results on the CR charge state model

Our proposed approach was tested and compared with Neural ODE [10] and DeepONet [15] approaches. Figure 9 shows a comparison of the average point-wise relative error, calculated via 49, for each method when applied to the test dataset. For this problem we see that the error produced by our proposed method is an order of magnitude lower than DeepONet [15]. Figure 9 also shows that Neural ODE performs poorly for this problem. Further, the left plot in figure 9 depicts a simulated trajectory for the proposed approach for a particular set of parameters, $\mathbf{p}$, from the test dataset, where we clearly see that the predicted solution matches closely to the one calculated by the numerical solver.

Expanding Latent Space and Hidden Dimension

Figure 10 shows the change in training and test loss when different architectures are chosen. For the latent expansion, all network hidden layers were held at 100 neurons, while the latent dimension was allowed to vary. The latent dimension variable represents how many times greater in dimension the latent space is than the original problem dimension. For the hidden expansion, the latent dimension multiplier was kept at one, indicating no change in problem dimensionality, while the hidden layers were allowed to vary in number of neurons. The result shows that much greater gains in accuracy are achieved by expanding the problem dimension to a higher dimensional latent space, even by only a small multiplier, in comparison to expanding the dimension of hidden layers, while not allowing for latent expansion, which resulted in very little gain in accuracy. It should be noted that expanding the latent dimension by too great of a multiplier will hurt the accuracy of the model.

Results on the full CR model

To reduce the memory requirements associated with training the full CR model, we use 4096 data samples for training and 2500 samples were reserved for testing purposes (test data set).

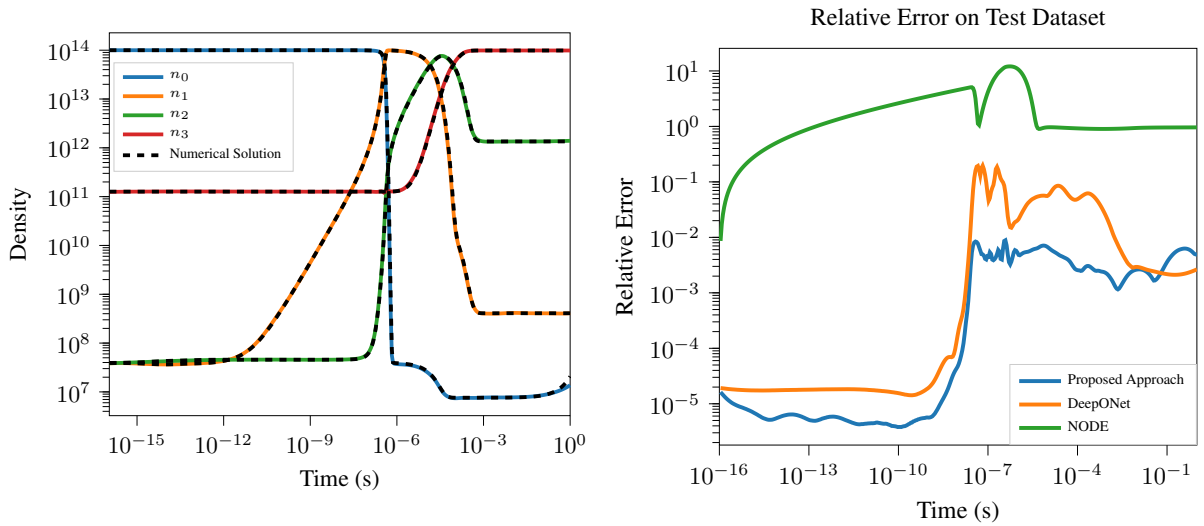

Figure 9: Left to Right: Comparison between numerical solution and machine learning prediction by the proposed approach for one set of test initial conditions and parameters for CR charge state model (section 3.2); Average point-wise relative error over time (49) when evaluating CR charge state model on test data.

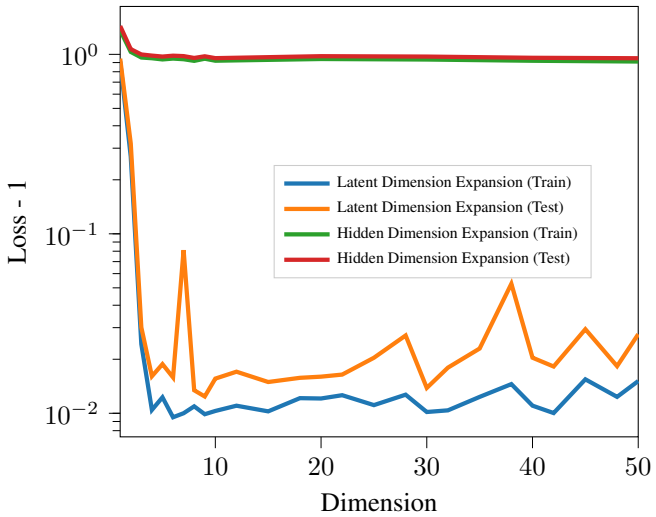

Figure 10: Training and testing loss obtained by architectures of varying latent and hidden dimension.

Figure 11 shows a comparison of the average point-wise relative error, calculated via 49, for each method when applied to the test dataset. We see that our proposed method outperformed DeepONet [15]. Further, for this higher-dimensional problem, training a Neural ODE network was not computationally feasible on our hardware (360 - NVIDIA Quadro RTX 5000) due to high memory requirements, even with the reduced training data set size. Hence, results for Neural ODE approach are not presented here. Further, the left plot in figure 11 depicts a simulated trajectory for the proposed approach for a particular set of parameters, $\mathbf{p}$, from the test dataset, where we clearly see that the predicted solution matches closely to the one calculated by the numerical solver.

Again, for both of the CR problems, the average error achieved by different machine learning methods has been tabulated in table 1 and additional results on the speedup achieved over the chosen traditional numerical solver (BDF6 method) have been tabulated in table 2.

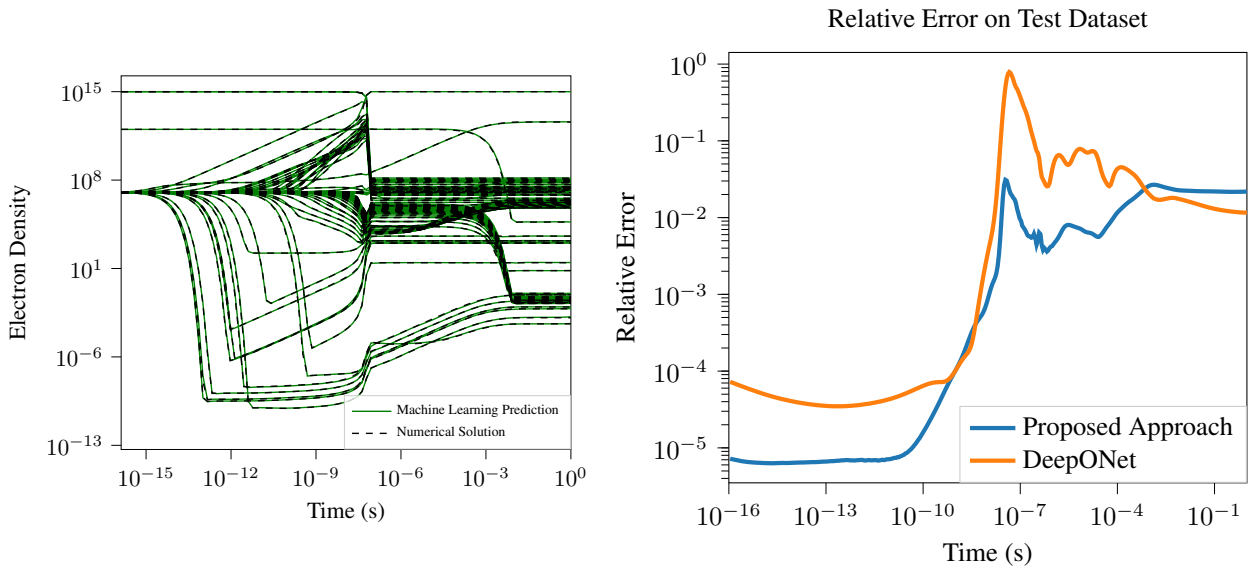

Figure 11: Left to Right: Comparison between numerical solution and machine learning prediction by the proposed approach for one set of test initial conditions and parameters for full CR model (section 3.2); Average point-wise relative error over time (49) when evaluating the full CR model on test data.

3.3 Allen-Cahn PDE in 1D

The governing equation for the Allen-Cahn problem [3] is given below:

$$u_t = \varepsilon u_{xx} + u - u^3, \tag{39}$$

where the solution is $u(x,t)$. The equation describes phase separation in iron alloys and has a second order diffusive term and a cubic reaction term [3]. In order to write (39) in the form (1), the spatial domain is discretized and integrated as a system of ODEs by the method of lines [32]. The spatial domain, $x \in [0, 2\pi]$ is discretized by 201 linearly spaced points. In the below discussions, $\mathbf{x}$ denotes the vector containing the ordered set of discrete points on the spatial domain.

3.3.1 Data Generation

Initial conditions are generated using a sum of three sinusoidal waves as follows:

$$\mathbf{u}_0 = \sum_{i=1}^{3} \alpha sin(\beta \mathbf{x} + \phi) + \alpha cos(\beta \mathbf{x} + \phi) \tag{40}$$

$$\alpha \sim \mathcal{U}(0, 1/6),\ \beta \sim \mathcal{U}_{discrete}(1, 3),\ \phi \sim \mathcal{U}(0, 2\pi), \tag{41}$$

where $\mathcal{U}$ represents the continuous uniform distribution and $\mathcal{U}_{discrete}$ denotes the discrete uniform distribution. The amplitude α and phase ϕ are sampled from continuous uniform distributions, while the frequency β of each wave is sampled from a discrete uniform distribution where the frequencies 1, 2, or 3 are the discrete choices, each with equal probability of being selected. The integer frequencies ensure that the solution, $\mathbf{u}$, is periodic on the problem domain. After the construction of the initial conditions, each initial condition is evolved in time using the ETDRK4 explicit, exponential integrator proposed in [33]. The problem is solved over the time interval $t \in [0, 10]$ seconds, which is discretized by 101 linearly spaced points, (i.e. $M = 101$ in (4)). The dataset contains 900 samples for training, 100 samples for validation, and an additional 200 test samples, where each sample is a complete time-integrated trajectory from a random initial condition generated by (40).

3.3.2 Results

The results for this problem are presented in figure 12. The left plot in figure 12 shows a solution generated by numerical code, while the middle plot in figure 12 shows the solution produced by our method, from the same initial condition, which was not seen during training. We observe that the solutions appear nearly identical. Finally, the right plot in

figure 12 shows the absolute point-wise error between our approach and the numerical code for the example initial condition. In terms of performance over the entire test set, figure 13 depicts the average error over time, in the relative L2 norm, for the three machine learning approaches. Each approach is trained with the same data, hyperparameter settings, and approximately the same total number of trainable parameters. We observed that our proposed approach outperformed both NODE and DeepONet for prediction on the Allen-Cahn PDE.

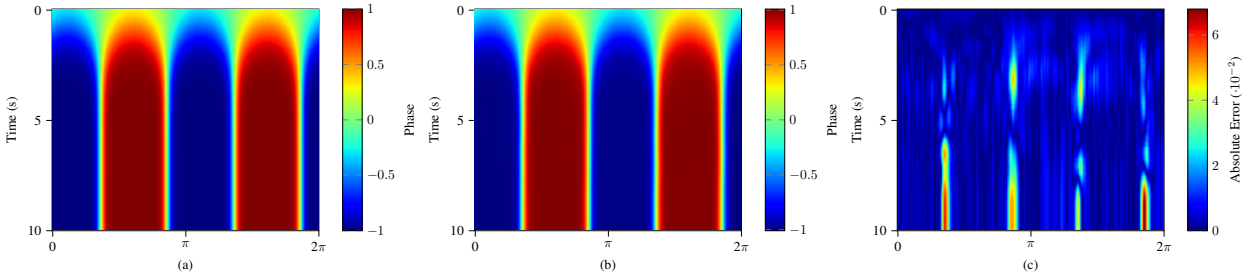

Figure 12: Left to right: Prediction by numerical method for Allen-Cahn PDE (section 3.3); Prediction by machine learning approach; Point-wise absolute error between the two approaches.

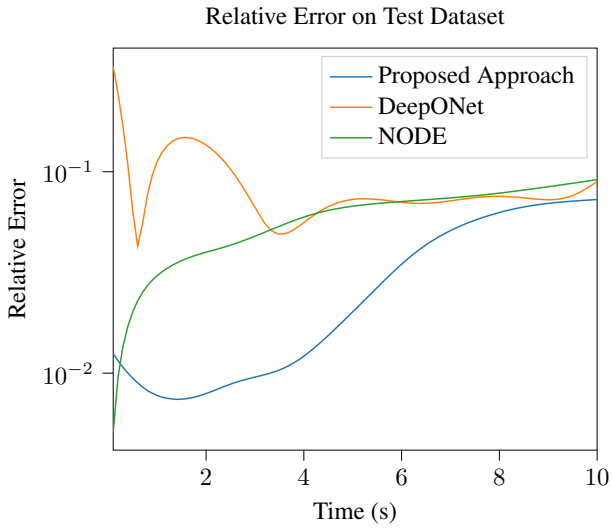

Figure 13: Average point-wise relative error over time (49) when evaluating Allen-Cahn PDE (section 3.3) on test data, for three machine learning approaches.

The average error achieved by different machine learning methods, for the Allen-Cahn PDE, are included in table 1. Speedup achieved over the chosen traditional numerical solver (ETDRK4 method) have, again, been tabulated in table 2.

3.4 Cahn-Hilliard PDE in 1D

The governing equation for the Cahn-Hilliard problem [3] is given below:

$$u_t = \alpha\left(-u_{xx} - \gamma u_{xxxx} + (u^3)_{xx}\right) \tag{42}$$

where the solution is $u(x,t)$. This is another equation describing phase separation in alloys, but with much more complex physics due to the presence of the higher-order derivatives in the governing equations. Just as with the Allen-Cahn problem (section 3.3), the spatial domain is discretized and integrated as a system of ODEs by the method of lines [32]. The spatial domain, $x \in [-1, 1]$ is discretized by 201 linearly spaced points, and is denoted by $\mathbf{x}$ in the below discussions.

3.4.1 Data Generation

Initial conditions in the Cahn-Hilliard problem are generated as follows:

$$\mathbf{u}_0 = \alpha sin(\beta\pi(\mathbf{x}+1) + \phi) + \alpha cos(\beta\pi(\mathbf{x}+1) + \phi), \tag{43}$$

$$\alpha \sim \mathcal{U}(0.1, 0.6),\ \beta \sim \mathcal{U}_{discrete}(1, 3),\ \phi \sim \mathcal{U}(0, 2\pi), \tag{44}$$

where $\mathcal{U}$ represents the continuous uniform distribution and $\mathcal{U}_{discrete}$ denotes the discrete uniform distribution. For each initial condition, generated by (43), the amplitude α and phase ϕ are sampled from continuous uniform distributions, specified in (44), while the frequency coefficient β of the wave is sampled from a discrete uniform distribution where the frequencies 1, 2, or 3 are the discrete choices, each with equal probability of being selected. The integer frequencies ensure that the solution, $\mathbf{u}$, is periodic on the problem domain. After the construction of the initial conditions, each initial condition is evolved in time using the ETDRK4 explicit, exponential integrator proposed in [33]. The problem is solved over the time interval $t \in [0, 20]$ seconds, which is discretized by 401 linearly spaced points (i.e. M = 401 in (4)). The dataset contains 900 samples for training, 100 samples for validation, and an additional 200 test samples, where each sample is a complete time-integrated trajectory from a random initial condition generated by (43).

3.4.2 Results

The results for this problem are presented in figure 14. The left plot in figure 14 shows a solution generated by numerical code, while the middle plot in figure 14 shows the solution produced by our method, from the same initial condition that was not seen during training. The right figure in figure 14 shows the absolute point-wise error between our approach and the numerical code for the example initial condition considered. In terms of performance over the entire test set, figure 15 depicts the average error over time, in the relative L2 norm, for the three machine learning approaches. Each approach is trained with the same data, hyperparameter settings, and approximately the same total number of trainable parameters. We observed that our proposed approach outperformed both NODE and DeepONet for prediction on the Cahn-Hilliard PDE.

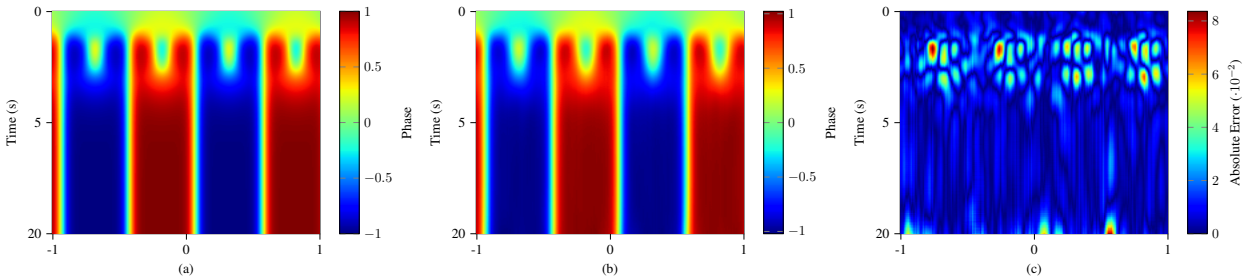

Figure 14: Left to right: Prediction by numerical method for Cahn-Hilliard PDE (section 3.4); Prediction by machine learning approach; point-wise absolute error between the two approaches.

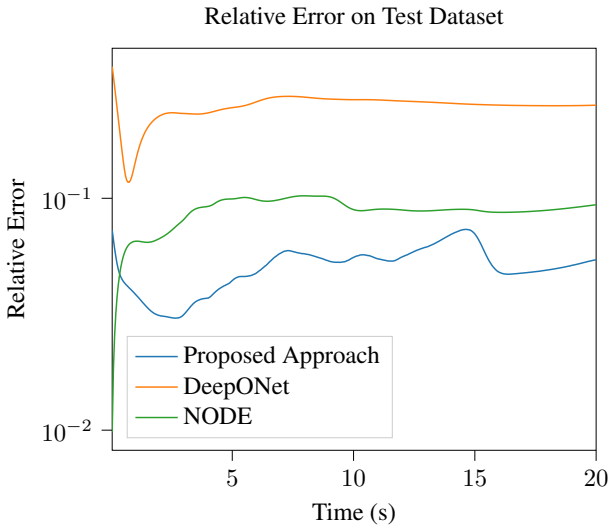

Figure 15: Average point-wise relative error over time (49) when evaluating Cahn-Hilliard PDE (section 3.4) on test data, for three machine learning approaches.

The average error achieved by different machine learning methods, for the Cahn-Hilliard PDE, are included in table 1. Speedup achieved over the chosen traditional numerical solver (ETDRK4 method) have, again, been tabulated in table 2.

3.5 Data Reduction

In this section, two methods of data reduction are considered and tested numerically. The first method of data reduction is the simple and obvious approach of reducing the number of sample trajectories (i.e. the parameter N in (4)) supplied to the model during training. The second method of data reduction is based on a coarsening of the time discretization in training data, (i.e. reducing the parameter M in (4)).

3.5.1 Reduced Training Sample Size

The effect of reducing the total number of sample trajectories for each ODE problem (sections 3.1 and 3.2) on the relative error are shown in figure 16. For the Robertson and full CR models (sections 3.1 and 3.2), the original network was trained with 4096 samples from a three-dimensional parameter space. To understand how the prediction accuracy degrades with training data size, several smaller datasets were created by repeatedly reducing the number of training samples by a factor of two. For the CR charge state model (section 3.2), the initial training utilized 15625 samples from a three-dimensional parameter input space. For this problem, smaller datasets were created by repeatedly reducing the number of training samples, this time by a factor of five. The smallest dataset, for each ODE problem considered, contained only the eight corners of the original 3-dimensional parameter space. For the Robertson model (section 3.1), with only 128 samples, we observed that a network can be trained to achieve error on the same order of magnitude as a network of the same architecture trained with 4096 samples (a reduction of 32x). For the CR charge state model, with only 125 samples, a network can be trained to achieve error on the same order of magnitude as a network of the same architecture trained with 15625 samples. For the full CR model, after 256 training samples, the network's final accuracy on the test dataset does not significantly improve.

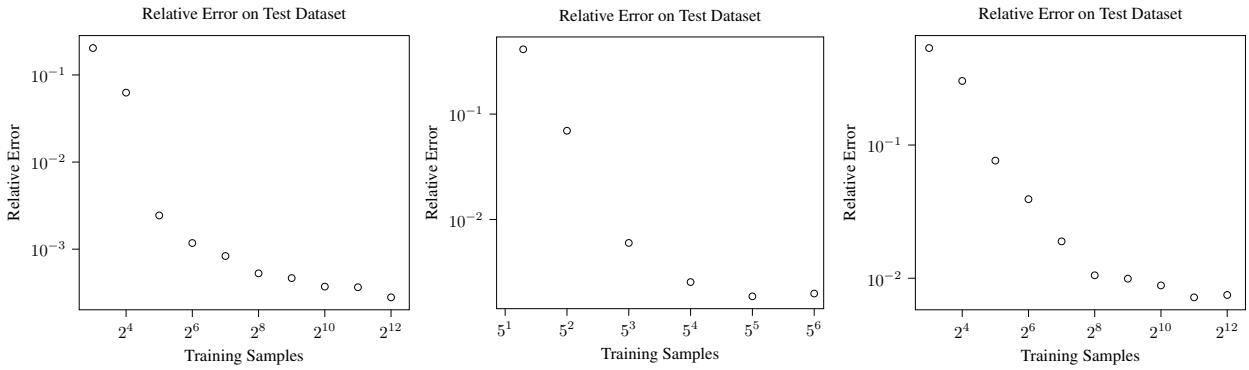

Figure 16: Left to Right: Average point-wise relative error over time (50) when evaluating ROBER chemical kinetics model (section 3.1) on test data (each plotted point shows the accuracy in relation to the number of training samples); Average point-wise relative error over time (50) when evaluating CR charge state model (section 3.2) on test data; Average point-wise relative error over time (50) when evaluating full CR model (section 3.2) on test data.

For completeness, the same sample reduction experiment was performed on each of the two PDE problems (sections 3.3 and 3.4. In each case, the original dataset of 900 samples was repeatedly reduced by 100 samples and used to train a new model. The smallest dataset contained 100 total sample trajectories. The change in accuracy with respect to sample size is shown in figure 17. On each of the PDEs, adding more samples typically results in a significant increase in accuracy, thus for these problems, a large number of samples may be necessary.

3.6 Importance of Learned Time Transformation

An additional strategy to reduce the data and memory requirements of training the network is to consider a coarse time grid for training the network. In this section, we consider different time discretizations by removing large numbers of time steps from the training and validation data and using this new dataset to train the networks. Examples of different time grids considered for training neural networks are shown in figures 18, 19, 20, 21, and 22 (left side). For assessing the performance, we retain the original test data, which has a fine discretization in time. Further, to demonstrate the

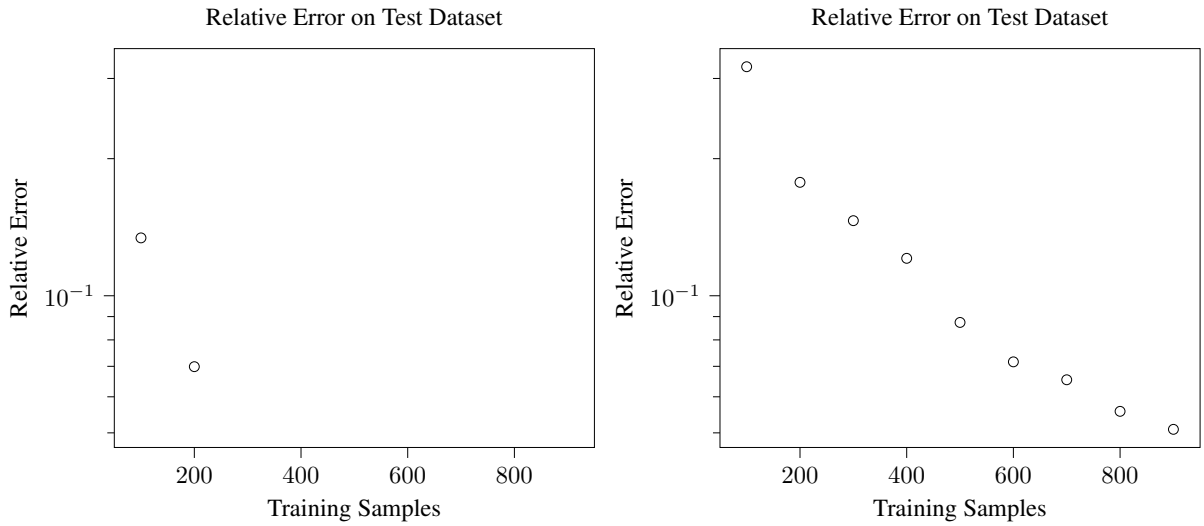

Figure 17: Left to Right: Average point-wise relative error over time (50) when evaluating Allen-Cahn PDE (section 3.3) on test data (each plotted point shows the accuracy in relation to the number of training samples); Average point-wise relative error over time (50) when evaluating Cahn-Hilliard PDE (section 3.4) on test data (each plotted point shows the accuracy in relation to the number of training samples) (50) on test data.

importance of nonlinear time transformation $\boldsymbol{\tau}\,(t,\ \boldsymbol{x}_0,\ \mathbf{p};\ \boldsymbol{\nu})$ in (3), we also consider an approach that does not learn a time transformation. In particular, instead of (3) we consider the solution in the latent space to have the following form:

$$\boldsymbol{y}\,(t,\ \boldsymbol{x}_0,\ \mathbf{p}) = \boldsymbol{\mathcal{E}}(\boldsymbol{x}_0, \mathbf{p};\ \boldsymbol{\beta}) + t\boldsymbol{\mathcal{C}}(\boldsymbol{x}_0, \mathbf{p};\ \boldsymbol{\alpha}). \tag{45}$$

where time is scaled between 0 and 1. The red dots in figures 18, 19, 20, 21, and 22 (right side) denotes the error achieved when one does not use a learned time transformation.

In all experiments, we ensured that each network had approximately the same number of parameters. The main purpose of this study is to investigate whether coarsening the discretization in time is an effective means to reduce data, while maintaining test accuracy in our approach. The results of our experiments are shown in figures 18, 19, 20, 21, 22. For the Robertson model and full CR model (right side figures 18, 20) we do not see significant advantages in the use of time transformation $\boldsymbol{\tau}\,(t,\ \boldsymbol{x}_0,\ \mathbf{p};\ \boldsymbol{\nu})$. However, for all other problems (right side figures 19, 21, 22) we see that the learning the time transformation $\boldsymbol{\tau}\,(t,\ \boldsymbol{x}_0,\ \mathbf{p};\ \boldsymbol{\nu})$ plays a vital role in achieving better generalization performance especially when using coarse time grids for training the networks.

4 Summary of results

Table 1 shows the prediction error computed using (50) for each machine learning method, on each problem. It is clear from Table 1 that our proposed approach outperforms the other considered approaches in terms of accuracy, on all problems. Further, Table 2 shows the speedup of the proposed approach in comparison to the traditional stiff numerical solver used to generate the data. To measure the speedup achieved, 1000 initial conditions were chosen to run the simulations. Table 2 shows the total time taken by the numerical solver and our proposed approach to compute the solutions for all the 1000 initial conditions. We see that our approach achieves $\mathcal{O}(10^1)$-$\mathcal{O}(10^3)$ speedup on all problems, in terms of wall clock computation time.

Table 1: Relative error on test data for the three machine learning approaches

Relative Error					
Problem	ROBER	CR charge state	Full CR model	Allen-Cahn	Cahn-Hilliard
Neural ODE	$1.112 \cdot 10^{-2}$	$2.209 \cdot 10^{0}$	**OOM**	$6.070 \cdot 10^{-2}$	$8.810 \cdot 10^{-2}$
DeepONet	$1.697 \cdot 10^{-3}$	$2.003 \cdot 10^{-2}$	$3.968 \cdot 10^{-2}$	$8.589 \cdot 10^{-2}$	$2.492 \cdot 10^{-1}$
Proposed Approach	$\mathbf{2.80 \cdot 10^{-4}}$	$\mathbf{1.981 \cdot 10^{-3}}$	$\mathbf{7.486 \cdot 10^{-3}}$	$\mathbf{1.072 \cdot 10^{-2}}$	$\mathbf{5.090 \cdot 10^{-2}}$

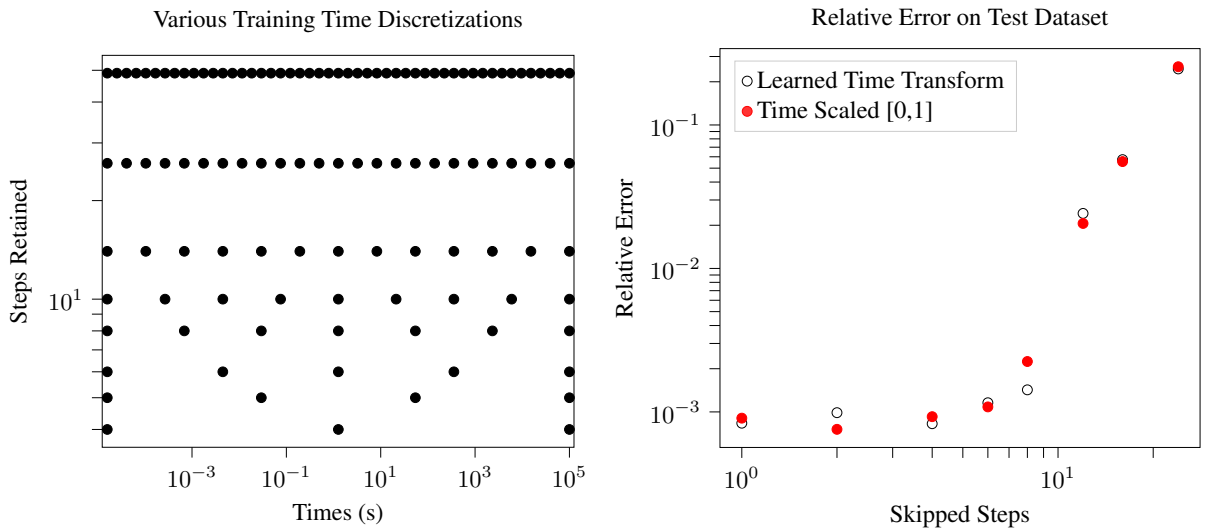

Figure 18: Effect of downsampling data in time (for training) on the prediction accuracy for the Robertson ODE (section 3.1). Left to Right: Examples of different time grids considered for training neural networks; Average point-wise relative error over time (50) on the test data.

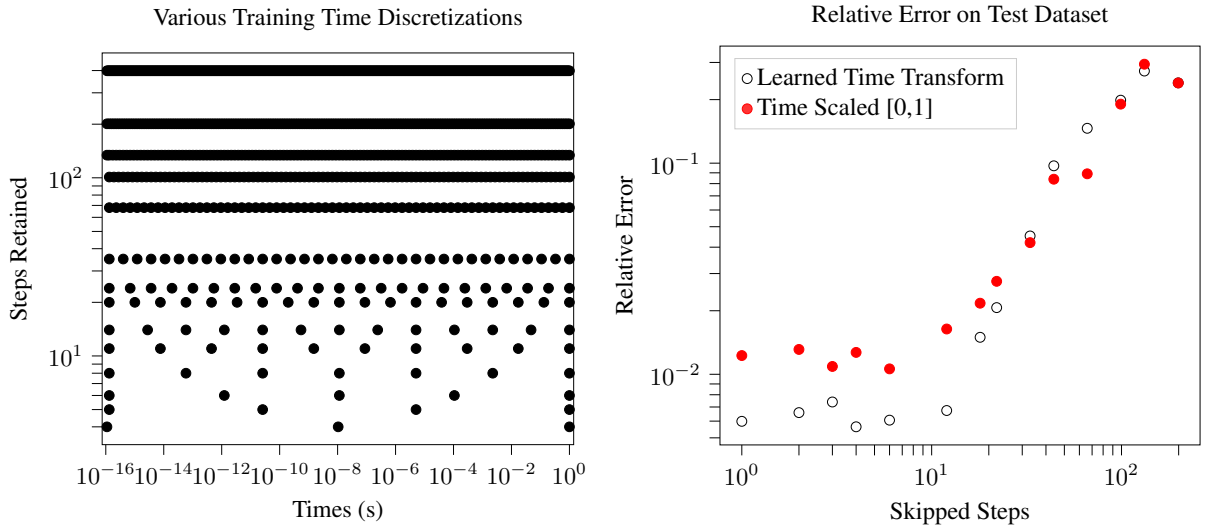

Figure 19: Effect of downsampling data in time (for training) on the prediction accuracy for CR charge state model (section 3.2). Left to Right: Examples of different time grids considered for training neural networks; Average point-wise relative error over time (50) on test data.

Table 2: Wall clock time comparison of our proposed approach with traditional numerical solver

Speed tests in wall clock time					
Problem	ROBER	CR charge state	Full CR model	Allen-Cahn	Cahn-Hilliard
Numerical Solver	6232.8s	11034.1s	10955.5s	53.25s	212.1s
Proposed Approach	7.648s	7.366s	13.604s	3.729s	15.485s
Speedup	**815.0x**	**1498.0x**	**805.3x**	**14.3x**	**13.7x**

5 Conclusion

In this paper, we have presented a novel, machine learning based approach for fast simulation of stiff, nonlinear, ordinary differential equations. Our approach involved learning a latent dynamical system with constant velocity, whose solution

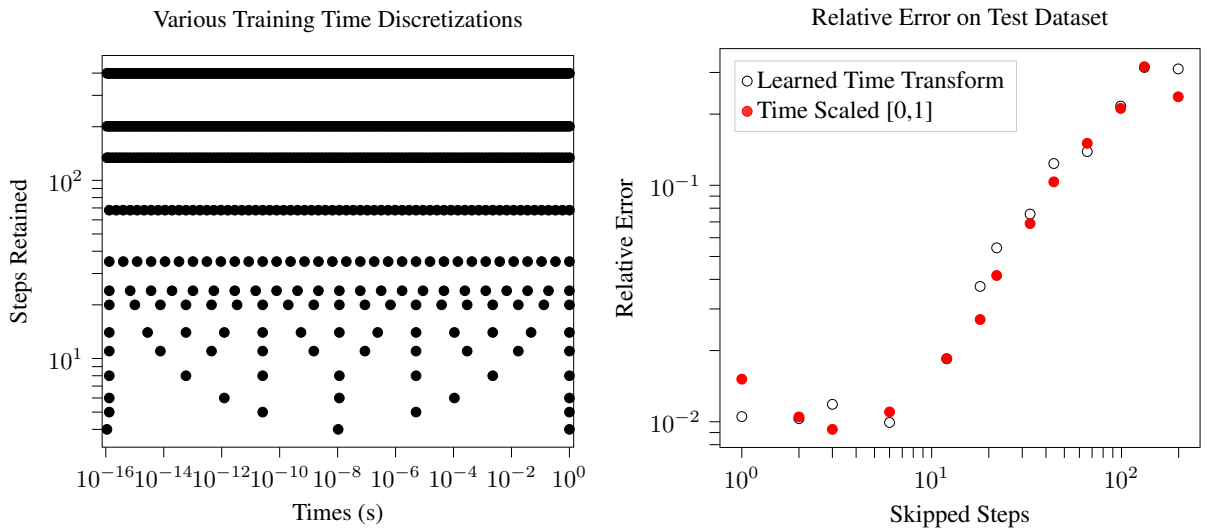

Figure 20: Effect of downsampling data in time (for training) on the prediction accuracy for the full CR model (section 3.2). Left to Right: Examples of different time grids considered for training neural networks; Average point-wise relative error over time (50) when evaluating full CR model on test data.

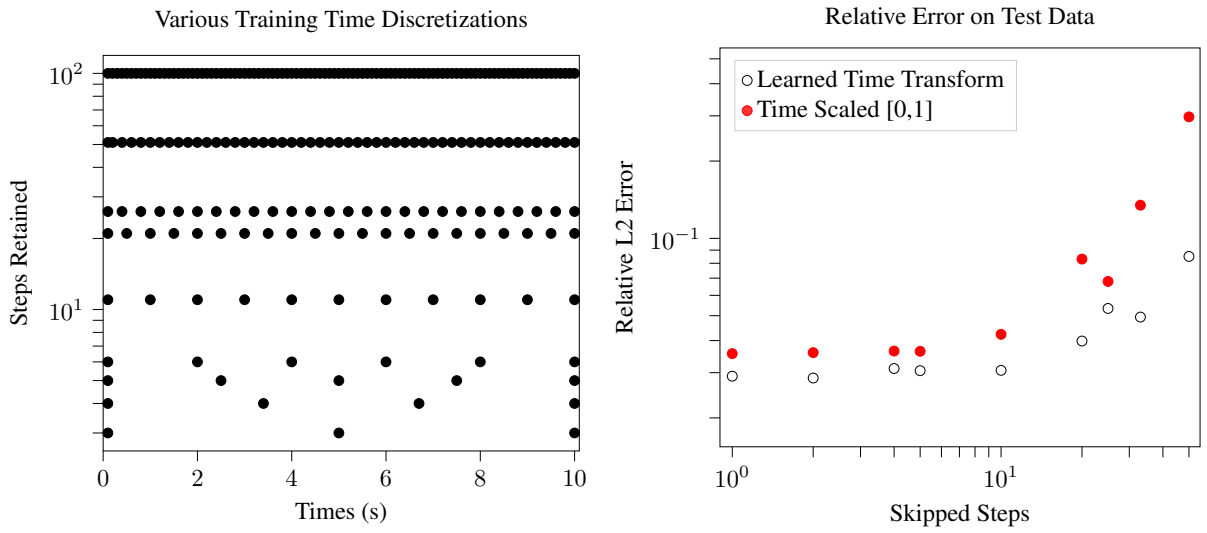

Figure 21: Effect of downsampling data in time (for training) on the prediction accuracy for the Allen-Cahn PDE (section 3.3). Left to Right: Examples of different time grids considered for training neural networks; Average point-wise relative error over time (50) on test data.

can be decoded to generate the solution to the original dynamical system. Note that the computational efficiency in this approach is attributed to the fact that one completely avoids numerical integration in the latent space. Further, we have also provided theoretical results justifying our approach. The effectiveness of the proposed method has been numerically demonstrated on several problems with varying dimensionality and complex, stiff behaviors. For each problem, in comparison to traditional stiff integrators, we observed that our proposed approach showed massive wall clock time reduction in simulating the stiff systems.

Furthermore, in section 2.1, we demonstrated that in scenarios where typical networks may fail to adequately learn the flow map of a dynamical system, our proposed method is an effective alternative, while also exhibiting better generalization capabilities. Our future work will focus on additional theoretical analysis (non-asymptotic analysis) to investigate the unanswered question of why our approach outperforms direct flow map learning, as demonstrated in section 2.1. In addition, in section 3.6 we showed that the nonlinear transformation of time in the latent space plays

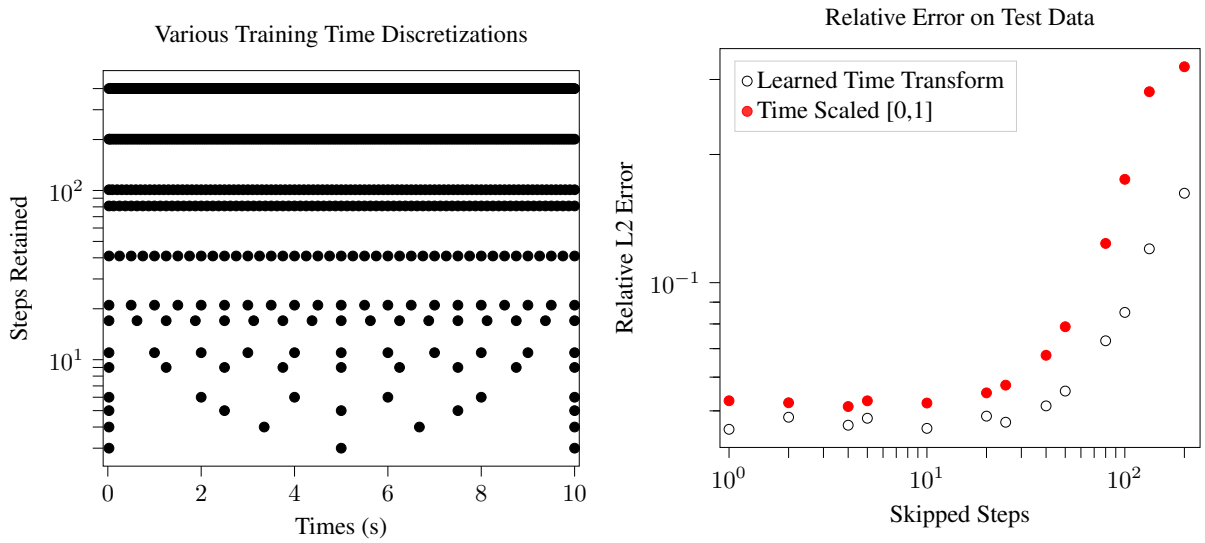

Figure 22: Effect of downsampling data in time (for training) on the prediction accuracy for the Cahn-Hilliard PDE (section 3.4). Left to Right: Examples of different time grids considered for training neural networks; Average point-wise relative error over time (50) on test data.

a vital role in achieving better generalization performance especially when using coarse time grids for training the networks.

Note that for high dimensional problem, data generation may not be cheap. Therefore, our future work will develop algorithms for adaptive data sampling (active learning) to reduce the amount of data required to train each model, while also answering the question of finding the optimal neural network architecture (number of layers, number of neurons in each layer) for prediction [34].

References

[1] Ranjan Anantharaman, Yingbo Ma, Shashi Gowda, Chris Laughman, Viral Shah, Alan Edelman, and Chris Rackauckas. Accelerating simulation of stiff nonlinear systems using continuous-time echo state networks, 2021.

[2] H.-K Chung, M.H. Chen, W.L. Morgan, Yuri Ralchenko, and Richard Lee. Flychk: Generalized population kinetics and spectral model for rapid spectroscopic analysis for all elements. *High Energy Density Physics*, 1, 06 2005.

[3] Hadrien Montanelli and Niall Bootland. Solving periodic semilinear stiff pdes in 1d, 2d and 3d with exponential integrators, 2020.

[4] W.L. Miranker. *The Computational Theory of Stiff Differential Equations*. Publication mathématique d'Orsay ; no 219-7667. Université Paris XI, U.E.R. mathématique, 1976.

[5] Henry Dikeman, Hongyuan Zhang, and Suo Yang. Stiffness-reduced neural ode models for data-driven reduced-order modeling of combustion chemical kinetics. 01 2022.

[6] Suyong Kim, Weiqi Ji, Sili Deng, Yingbo Ma, and Christopher Rackauckas. Stiff neural ordinary differential equations. *Chaos: An Interdisciplinary Journal of Nonlinear Science*, 31(9), September 2021.

[7] Sifan Wang, Yujun Teng, and Paris Perdikaris. Understanding and mitigating gradient pathologies in physics-informed neural networks, 2020.

[8] Hai V Nguyen and Tan Bui-Thanh. A model-constrained tangent slope learning approach for dynamical systems. *International Journal of Computational Fluid Dynamics*, 36(7):655–685, 2022.

[9] Hai Van Nguyen, Jau-Uei Chen, , and Tan Bui-Thanh. A model-constrained discontinuous galerkin network (dgnet) for compressible euler equations with out-of-distribution generalization. *arXiv preprint arXiv:2409.18371*, 2024.

[10] Kookjin Lee and Eric J. Parish. Parameterized neural ordinary differential equations: applications to computational physics problems. *Proceedings of the Royal Society A: Mathematical, Physical and Engineering Sciences*, 477(2253):20210162, September 2021.

[11] Tadbhagya Kumar, Anuj Kumar, and Pinaki Pal. A physics-constrained neuralode approach for robust learning of stiff chemical kinetics. 12 2023.

[12] Weiqi Ji, Weilun Qiu, Zhiyu Shi, Shaowu Pan, and Sili Deng. Stiff-pinn: Physics-informed neural network for stiff chemical kinetics. *The Journal of Physical Chemistry A*, 125(36):8098–8106, August 2021.

[13] Bethany Lusch, J. Nathan Kutz, and Steven L. Brunton. Deep learning for universal linear embeddings of nonlinear dynamics. *Nature Communications*, 9(1), November 2018.

[14] Omri Azencot, N. Benjamin Erichson, Vanessa Lin, and Michael W. Mahoney. Forecasting sequential data using consistent koopman autoencoders, 2020.

[15] Somdatta Goswami, Ameya D. Jagtap, Hessam Babaee, Bryan T. Susi, and George Em Karniadakis. Learning stiff chemical kinetics using extended deep neural operators, 2023.

[16] Elizaveta Levina and Peter J. Bickel. Maximum likelihood estimation of intrinsic dimension. In *Neural Information Processing Systems*, 2004.

[17] Evangelos Galaris, Gianluca Fabiani, Francesco Calabrò, Daniela di Serafino, and Constantinos Siettos. Numerical solution of stiff odes with physics-informed rpnns, 2021.

[18] Erik Bollt. On explaining the surprising success of reservoir computing forecaster of chaos? The universal machine learning dynamical system with contrast to VAR and DMD. *Chaos: An Interdisciplinary Journal of Nonlinear Science*, 31(1):013108, 01 2021.

[19] Kei Ota, Tomoaki Oiki, Devesh K. Jha, Toshisada Mariyama, and Daniel Nikovski. Can increasing input dimensionality improve deep reinforcement learning?, 2020.

[20] Hartmut Logemann, Eugene P Ryan, et al. *Ordinary differential equations: analysis, qualitative theory and control*. Springer, 2014.

[21] Patrick Kidger and Terry Lyons. Universal approximation with deep narrow networks. In *Conference on learning theory*, pages 2306–2327. PMLR, 2020.

[22] Immanuel Sulzer and Tobias Buck. Speeding up astrochemical reaction networks with autoencoders and neural odes, 2023.

[23] George F Simmons. *Differential equations with applications and historical notes*. CRC Press, 2016.

[24] Gerald Teschl. *Ordinary differential equations and dynamical systems*, volume 140. American Mathematical Society, 2024.

[25] Michael Spivak. *Calculus*. Cambridge University Press, 2006.

[26] John Denholm Lambert. Computational methods in ordinary differential equations. 1973.

[27] William E Boyce and Richard C DiPrima. *Elementary differential equations*, volume 9. Wiley New York, 2009.

[28] Anne Kværnø. Singly diagonally implicit runge–kutta methods with an explicit first stage. *BIT Numerical Mathematics*, 44(3):489–502, 2004.

[29] Patrick Kidger. *On Neural Differential Equations*. PhD thesis, University of Oxford, 2021.

[30] Nathan A Garland, Romit Maulik, Qi Tang, Xian-Zhu Tang, and Prasanna Balaprakash. Efficient data acquisition and training of collisional-radiative model artificial neural network surrogates through adaptive parameter space sampling. *Machine learning: science and technology*, 3(4):045003, 2022.

[31] E. Süli and D.F. Mayers. *An Introduction to Numerical Analysis*. An Introduction to Numerical Analysis. Cambridge University Press, 2003.

[32] William E. Schiesser. *The Numerical Method of Lines: Integration of Partial Differential Equations*. Elsevier, 2012.

[33] S.M. Cox and P.C. Matthews. Exponential time differencing for stiff systems. *Journal of Computational Physics*, 176(2):430–455, 2002.

[34] CG Krishnanunni, Tan Bui-Thanh, and Clint Dawson. Topological derivative approach for deep neural network architecture adaptation. *arXiv preprint arXiv:2502.06885*, 2025.

A General setting for numerical experiments

A.1 Data Transformations

ODE Problems: sections 3.1, 3.2

To address the multiscale nature of the data in the three ODE problems, as a preprocessing step, all time series data is log scaled using the base 10 logarithm. This procedure reduces the scale separation of different components of the solution. As an additional training aid, all network inputs, apart from time, are scaled independently to the range $[-1, 1]$. Finally, the time discretization points are log scaled, using the base 10 logarithm, and then rescaled to fit the range $[0, 1]$ seconds.

PDE Problems: sections 3.3, 3.4

For both PDE models, the data all lies on the range $[-1, 1]$, so no normalization is required. However, the the time discretization points are rescaled to fit the range $[0, 1]$ seconds.

A.2 Training for Multiscale Stiff Systems

In all of the ODE (sections 3.1 and 3.2) test problems presented in this paper, the unique degrees of freedom in the solution vary by several orders of magnitude. This led to challenges in training with traditional loss functions such as mean squared error (MSE). In training, such loss functions were heavily biased toward learning the large magnitude components of the solution. To remedy this issue, we considered an absolute relative error loss function. The use of relative error balances out the magnitudes of errors for each individual degree of freedom.

$$\mathcal{L}(\mathbf{X}; \boldsymbol{\alpha}, \boldsymbol{\beta}, \boldsymbol{\nu}, \boldsymbol{\theta}) = \frac{1}{(N+1)\cdot(M+1)} \sum_{i=0}^{N} \sum_{j=0}^{M} \left| \frac{[\mathbf{x}(t_j)]_i - [\hat{\mathbf{x}}(t_j)]_i}{[\mathbf{x}(t_j)]_i} \right|. \tag{46}$$

where, the predicted state $[\hat{\boldsymbol{x}}(t_j)]_i$ for time t_j and for the ith training input $\{(\boldsymbol{x}_0)_i, \mathbf{p}_i\}$ is given by (48). $[\boldsymbol{x}(t_j)]_i$ denotes the actual state at time t_j for the ith input. However, this loss function still has the problem that overshooting errors are punished much more harshly than undershooting errors. Finally, we settled on the following loss function which resolves the unbalanced penalties between overshooting and undershooting.

$$\mathcal{L}(\mathbf{X}; \boldsymbol{\alpha}, \boldsymbol{\beta}, \boldsymbol{\nu}, \boldsymbol{\theta}) = \frac{1}{N+1} \sum_{i=0}^{N} \prod_{j=0}^{M} 10^{\frac{1}{M+1} \left| [\mathbf{x}(t_j)]_i - [\hat{\mathbf{x}}(t_j)]_i \right|}, \tag{47}$$

$$[\hat{\mathbf{x}}(t_j)]_i = \mathcal{D}\left(\mathcal{E}((\mathbf{x}_0)_i, \mathbf{p}_i; \boldsymbol{\alpha}) + \boldsymbol{\tau}(t_j, (\mathbf{x}_0)_i, \mathbf{p}_i; \boldsymbol{\nu}) \circ \mathcal{C}(\mathbf{x}_{0_i}, \mathbf{p}_i; \boldsymbol{\beta}); \boldsymbol{\theta}\right). \tag{48}$$

In (47), $\mathbf{X}$ is a third order tensor containing $[\mathbf{x}(t_j)]_i$ for all samples, $s = 0, \ldots, N_s$, and all times, $t = 0, \ldots, N_t$, in the dataset. Similarly, $\mathbf{P}$ is a matrix containing the parameters, $\mathbf{p}_i$, for all samples.

The above loss function is used for the ODE problems which are trained using a log scaled version of the original data. For the PDE problems (sections 3.3 and 3.4), the data is not log scaled so a different loss function was chosen. We do not use an absolute error style loss function, since some of the true data is 0, meaning the relative error will be undefined at those points. Instead, the evaluation metric (50) was used as the loss function in training.

A.3 Error Evaluation Metrics

The plots, in this paper, depicting relative error over time, report the point-wise relative error in the Euclidean norm, averaged over all N samples, given as

$$\mathcal{R}_1 = \frac{1}{N+1} \sum_{i=0}^{N} \frac{\left|\left|[\mathbf{x}(t_j)]_i - [\hat{\mathbf{x}}(t_j)]_i\right|\right|_2}{\left|\left|[\mathbf{x}(t_j)]_i\right|\right|_2}. \tag{49}$$

Table 1 reports the point-wise relative error in the Euclidean norm, averaged over all N samples and M time steps, given as:

$$\mathcal{R}_2 = \frac{1}{(N+1)\cdot(M+1)} \sum_{i=0}^{N} \sum_{j=0}^{M} \frac{\left|\left|[\mathbf{x}(t_j)]_i - [\hat{\mathbf{x}}(t_j)]_i\right|\right|_2}{\left|\left|[\mathbf{x}(t_j)]_i\right|\right|_2}. \tag{50}$$

A.4 Description of methods adopted for comparison

Our proposed approach is compared with two different approaches as described below:

DeepONet : An operator learning approach with branch networks, taking the state as its input, and trunk networks, taking time as its input, with the inner product of their respective outputs being the predicted solution, as described in [15].

Neural ODE : A scheme for approximating the right hand side of a parameterized ODE with a neural network and and solving using traditional numerical integration schemes, as described in [10]. The solver used with the neural ODEs implemented in our work is an implicit backward Euler scheme.

A.5 Architectural Details

Below are the neural network architectures used for each machine learning method and problem setting. Each network uses the $Tanh$ activation function at each hidden layer and has a linear output layer. The notation, [*,...,*], indicates the number of neruons in each layer for a multilayer preceptron network, including the initial input layer. The $\boldsymbol{\tau}$ networks have an additional number of parameters due to their special form, explained in equation (16). Recall that, since we use the independent architectural variants for testing each ODE problem, there is one network of each type per degree of freedom in the system of ODEs for the proposed approach and DeepONet. Networks following the "independent" architectural variant from section 2.3 are labeled with a $*$ in the following table. All other networks are implemented as the "full" variant from section 2.3. The labels (DR1) and (DR2) denote the architectures which were used in the data reduction experiments, described in section 3.5. The label (DR1) indicates our approach, while (DR2) indicates the ommision of the time transform. For problems, in the table without a (DR1) entry, the same architecture used in section 3 was used for the data reduction experiments.

Proposed Approach					
Problem	Encoder $\mathcal{E}$	Encoder $\mathcal{C}$	Encoder $\boldsymbol{\tau}$	Decoder $\mathcal{D}$	Total Parameters
ROBER*	[3,20,5]	[3,20,5]	[4,20,5], 5	[5,20,20,1]	$3,423$
ROBER* (DR2)	[3,23,5]	[3,23,5]	N/A	[5,23,23,1]	$3,414$
CR Charge States*	[3,20,5]	[3,20,5]	[4,20,5], 5	[5,20,20,1]	$4,564$
CR Charge States* (DR2)	[3,23,5]	[3,23,5]	N/A	[5,23,23,1]	$4,552$
Full CR*	[3,40,20]	[3,40,20]	[4,40,20], 20	[20,40,40,1]	$518,974$
Full CR* (DR1)	[3,40,5]	[3,40,5]	[4,40,5], 5	[5,40,40,1]	$287,734$
Full CR* (DR2)	[3,44,5]	[3,44,5]	N/A	[5,44,44,1]	$290,554$
Allen-Cahn	[201,201,201]	[201,201,201]	[202,201,201], 201	[201,201,201,201]	$365,820$
Allen-Cahn (DR1)	[201,100,20]	[201,100,20]	[202,100,20], 20	[20,100,100,201]	$99,281$
Allen-Cahn (DR2)	[201,155,20]	[201,155,20]	N/A	[202,155,155,20]	$99,596$
Cahn-Hilliard	[201,201,201]	[201,201,201]	[202,201,201], 201	[201,201,201,201]	$365,820$
Cahn-Hilliard (DR1)	[201,100,20]	[201,100,20]	[20,100,201], 20	[20,100,100,201]	$99,281$
Cahn-Hilliard (DR2)	[201,155,20]	[201,155,20]	N/A	[20,155,155,201]	$99,596$

DeepONet			
Problem	Branch Network	Trunk Network	Total Parameters
ROBER	[3,20,20,5]	[1,20,20,5]	$3,510$
CR Charge States	[3,20,20,5]	[1,20,20,5]	$4,680$
Full CR	[3,42,42,20]	[1,42,42,20]	$524,896$
Allen-Cahn	[201,8,8,8]	[1,8,8,8]	$356,976$
Cahn-Hilliard	[201,8,8,8]	[1,8,8,8]	$356,976$

Neural ODE		
Problem	Network	Total Parameters
ROBER	[6,39,39,39,3]	$3,513$
CR Charge States	[7,45,45,45,4]	$4,684$
Allen-Cahn	[201,338,338,338,201]	$365,579$
Cahn-Hilliard	[201,338,338,338,201]	$365,579$

A.6 Hyperparameter Settings

Below is a table, listing the hyperparameter settings used in training for each method and problem setting. In each ODE problem, the batch size is approximately 5% of the total samples. In the PDE problems (sections 3.3 and 3.4), the entire training set is given to the network as a single batch. The label (DR) in the table indicates the hyperparameter setting used in section 3.6, which contains experiments on coarsening the time discretization of training data.

Training Hyperparameter Settings				
Problem	Learning Rate	Training Samples	Batch Size	Training epochs
ROBER	10^{-5}	$4,000$	50	$10,000$
ROBER (DR)	10^{-5}	128	6	$10,000$
CR Charge States	10^{-4}	$15,625$	781	$10,000$
CR Charge States (DR)	10^{-4}	125	6	$10,000$
Full CR	10^{-4}	$4,096$	204	$10,000$
Full CR (DR)	10^{-4}	256	12	$10,000$
Allen-Cahn	10^{-4}	900	900	$20,000$
Allen-Cahn (DR)	10^{-4}	900	900	$50,000$
Cahn-Hilliard	10^{-4}	900	900	$20,000$
Cahn-Hilliard (DR)	10^{-4}	900	900	$100,000$

A.7 Initialization Sensitivity Studies

A.7.1 Robertson Chemical Reaction ODE

For the Robertson ODE (section 3.1), we trained networks considering 100 random parameter initializations. In figure 23, the left plot shows the mean relative error over time (49) on a test dataset of 512 samples, while the right plot shows the width of the error band over time. The width of the error band generally stays on the same scale as the error.

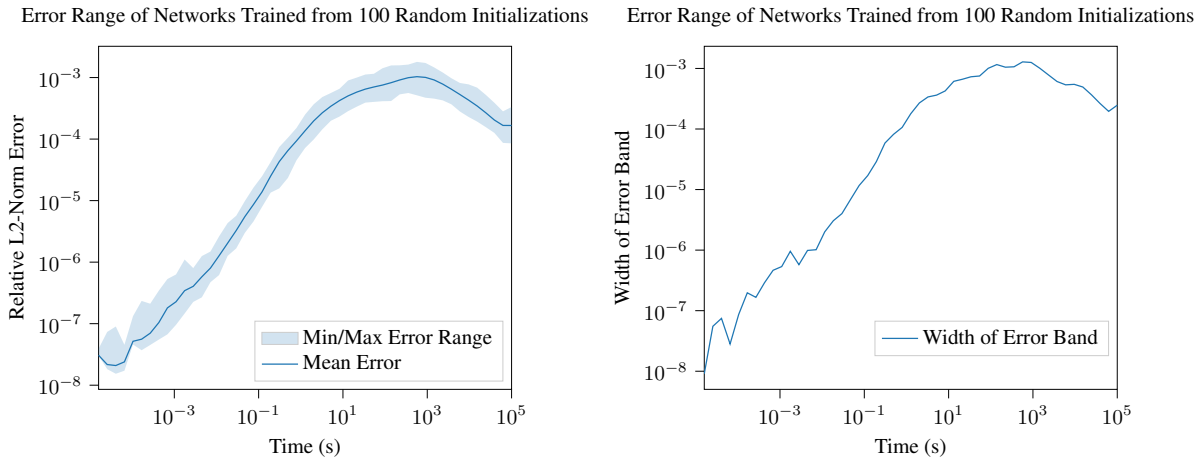

Figure 23: Left to Right: Mean relative error for Robertson ODE (section 3.1) test dataset, calculated by (49), across 100 random network parameter initializations, with min-max range; Maximum - Minimum error band width over time

A.7.2 Collisional-Radiative Model

For the CR charge state model (section 3.2), we, again, trained networks from 100 random parameter initializations. In figure 24, the left plot shows the mean relative error over time (49) on a test dataset of 4096 samples, while the right plot shows the width of the error band over time. The width of the error band generally stays on the same scale as the error.

For the full CR model (section 3.2), we trained networks from 15 random parameter initializations. Fewer networks were trained because the networks are much more costly to train on this problem. In figure 25, the left plot shows the mean relative error over time (49) on a test dataset of 2500 samples, while the right plot shows the width of the error band over time. The width of the error band generally stays on the same scale as the error.

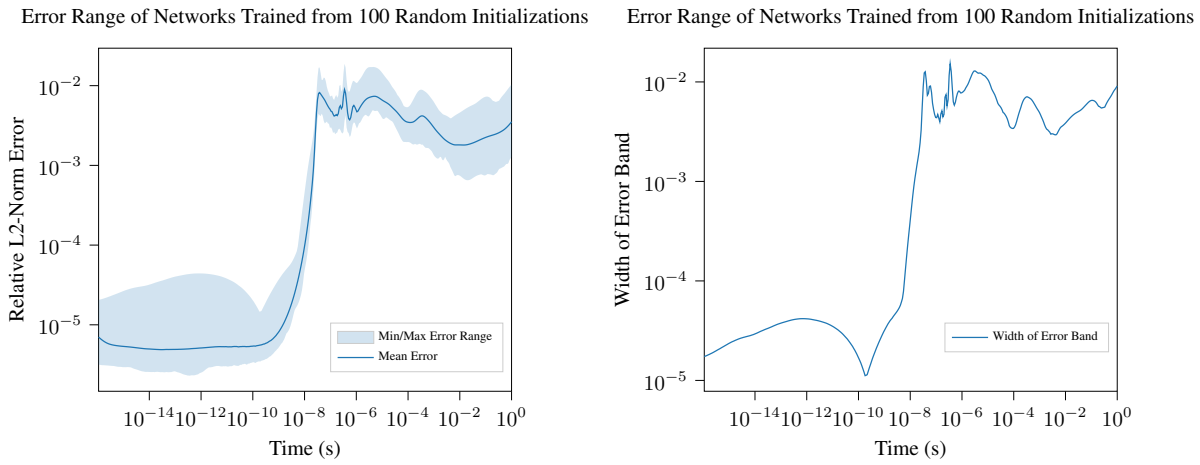

Figure 24: Left to Right: Mean relative error for CR charge state model (section 3.2) test dataset, calculated by (49), across 100 random network parameter initializations, with min-max range; Maximum - Minimum error band width over time

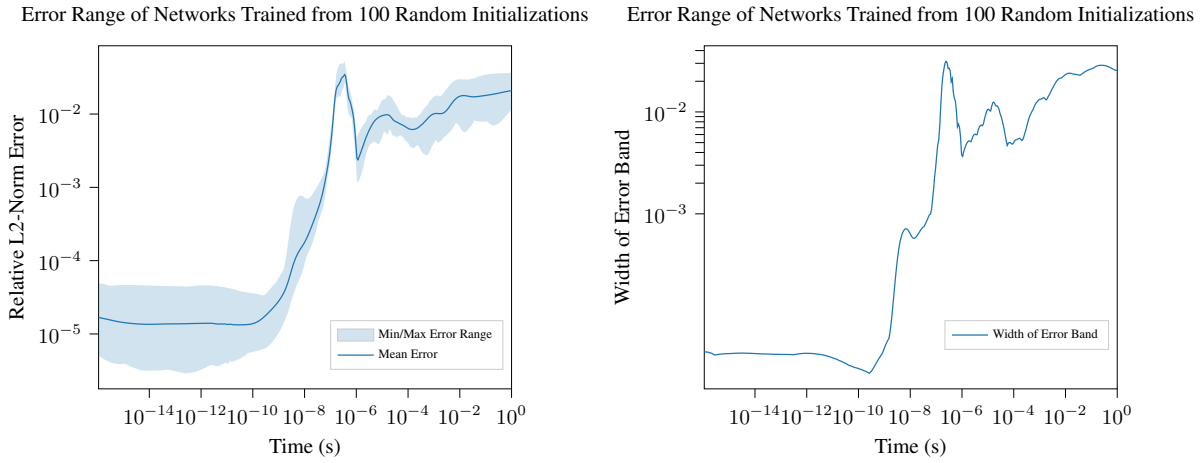

Figure 25: Left to Right: Mean relative error for full CR model (section 3.2) test dataset, calculated by (49), across 100 random network parameter initializations, with min-max range; Maximum - Minimum error band width over time

A.7.3 Allen-Cahn PDE

For the Allen-Cahn PDE (section 3.3), we trained networks from 100 random parameter initializations. In figure 26, the left plot shows the mean relative error over time (49) on a test dataset of 200 samples, while the right plot shows the width of the error band over time. The width of the error band generally stays on the same scale as the error.

A.7.4 Cahn-Hilliard PDE

For the Cahn-Hilliard PDE (section 3.4), we trained networks from 100 random parameter initializations. In figure 27, the left plot shows the mean relative error over time (49) on a test dataset of 200 samples, while the right plot shows the width of the error band over time. The width of the error band generally stays on the same scale as the error.

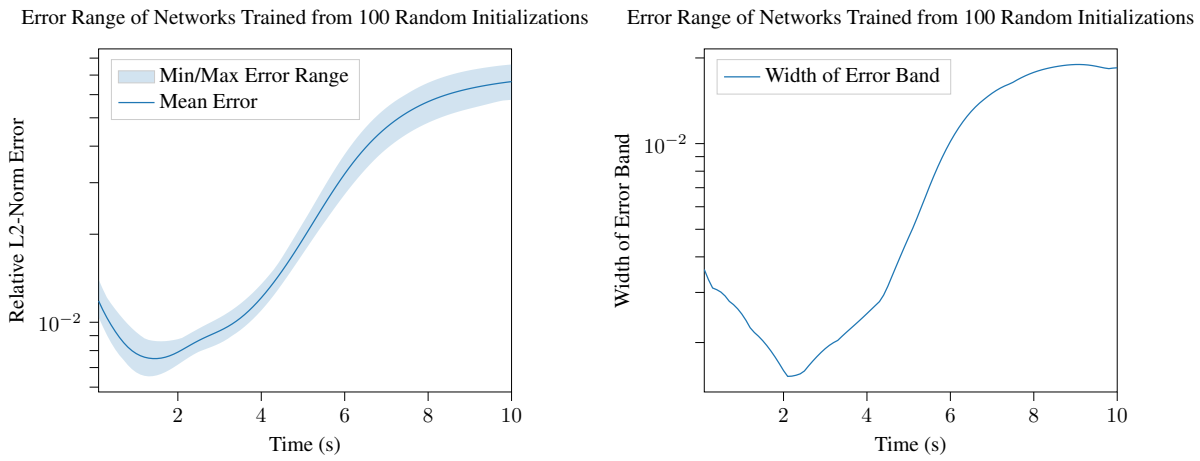

Figure 26: Left to Right: Mean relative error for Allen-Cahn (section 3.3) test dataset, calculated by (49), across 100 random network parameter initializations, with min-max range; Maximum - Minimum error band width over time

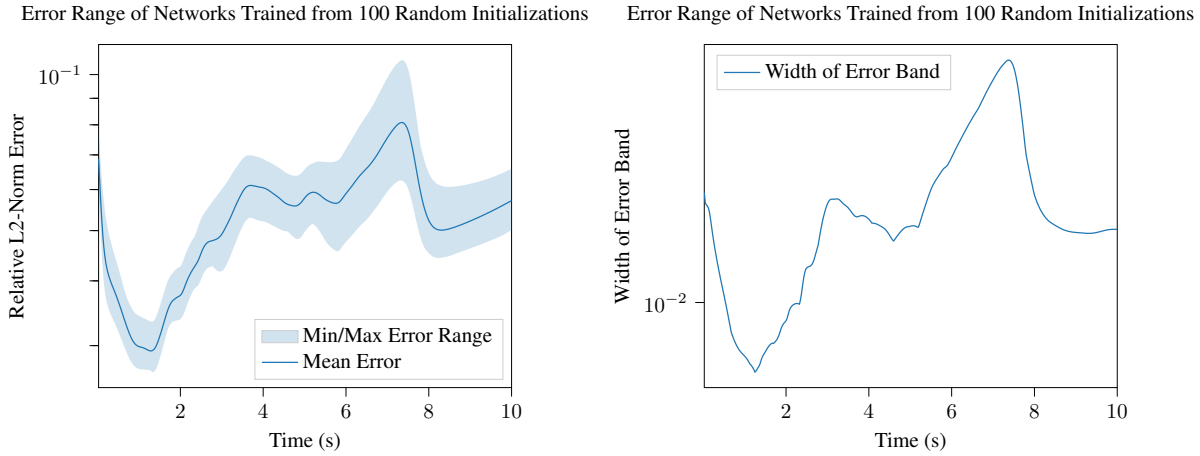

Figure 27: Left to Right: Mean relative error for Cahn-Hilliard (section 3.4) test dataset, calculated by (49), across 100 random network parameter initializations, with min-max range; Maximum - Minimum error band width over time